

Chapter 7

Dynamic Measurements of Magnetoelectricity in Metglas-Piezocrystal Laminates

João V. Vidal, Andrey A. Timopheev, Andrei L. Kholkin
and Nikolai A. Sobolev

Abstract This chapter describes an experimental technique, developed experimental setup and respective experimental study of the dynamic properties of direct magnetoelectric (ME) effect measured in metglas-piezocrystal laminates. We have prepared a variety of different magnetoelectric laminates by bonding magnetostrictive metglas foils onto single-crystalline substrates of LiNbO_3 (LNO), GaPO_4 (GPO) and PMN-PT. The measurements have been performed as a function of the crystal cut, magnitude and orientation of the magnetic bias field and the frequency of the modulation field. Despite much weaker PE coefficients of LNO and GPO, direct ME effects have been found to have comparative magnitudes in the samples based on them and on PMN-PT. Greatly enhanced ME coefficients in certain resonance modes are explored and their relations to the material properties of the crystals and the geometry of the composites are investigated. We demonstrate that control of the PE crystal's orientation can be successfully used in order to obtain almost any desired quasi-static and resonant anisotropic ME properties for some given application. Such unique features as chemical stability, linear piezoelectricity, thermal robustness open up a real perspective to use lead-free LNO and α -GPO based ME tri-layers, e.g., as vector magnetic field sensors working in a wide range of temperatures.

J.V. Vidal · A.A. Timopheev · N.A. Sobolev
Departamento de Física and I3N, Universidade de Aveiro, 3810-193 Aveiro, Portugal

A.L. Kholkin
Departamento de Física and CICECO, Universidade de Aveiro, 3810-193 Aveiro, Portugal

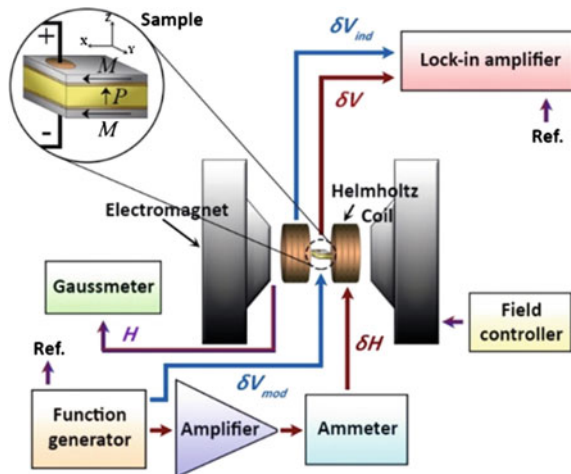
A.L. Kholkin
Institute of Natural Sciences, Ural Federal University, 620000 Ekaterinburg, Russia

N.A. Sobolev (✉)
National University of Science and Technology “MISiS”, 119049 Moscow, Russia
e-mail: sobolev@ua.pt

7.1 Introduction

The magnetoelectric (ME) effect, in its most general definition, describes any type of coupling between polarization and magnetic fields (direct effect) and conversely between magnetization and electric fields (converse effect) in matter. This effect has given rise to a lot of interest in the scientific community over the past few years [1–8]. Unlike the ME single-phase multiferroics, several ME composites, combining elastically coupled piezoelectric (PE) and magnetostrictive (MS) phases, have been shown to yield very strong ME effects even at room temperature [1–3]. These structures also offer a great flexibility in the sense that a large number of parameters may be adjusted independently including the material properties of the constituent phases as well as the connectivity arrangement between them. Consequently, nowadays these materials are already very close to some promising applications which include [1, 2, 5]: DC and AC magnetic vector field sensors and electric current sensors, magneto-electro-elastic energy harvesters, multiple-state memory devices, micro-sensors in read heads, transformers, spinners, diodes, spin-wave generators and electrically tunable microwave devices. The 2-2 type tri-laminated structures, among other the types of connectivity, comprising a layer of a PE material sandwiched between two layers of a MS phase, are characterized by a particularly rich anisotropy as well as an enhanced ME coupling due to both the absence of leakage currents and a strong mechanical coupling between phases [1–3]. Also, the transversal “L-T” operation mode, in which the MS phase is longitudinally magnetized while the PE layer is perpendicularly polarized (see Fig. 7.1), tends to maximize the exchange of strain between phases and also minimize the

Fig. 7.1 Schematic presentation of the experimental setup used to perform the ME measurements. Red and blue arrows are associated with the measurements of the direct and converse ME effects, respectively [30] (Color in online)



demagnetizing fields in the MS layer and is therefore the most commonly employed operation mode [1–3].

In the experimental quantification of the direct ME effect a dynamic direct ME voltage coefficient $\alpha_{Eij} = \partial E_i / \partial H_j$ (where E_i is the component of the electric field in the i direction and H_j is the component of the magnetic field in the j direction) is generally used as a figure of merit under open-circuit conditions (i.e. with a displacement field $D_i = 0$). Also, a large enhancement in the magnitude of the ME effect is expected whenever the frequency of an applied modulation magnetic field with amplitude (δH) matches one of the natural electrical, magnetic or mechanical modes of resonance of the composite [9–12]. For the case of the PE phase this is known as electromechanical (EM) resonance and it occurs whenever a characteristic elastic eigenmode of the PE phase is indirectly excited by the time varying magnetic field [10]. Thus, a large oscillation amplitude of the standing wave in this phase gives rise to a large polarization/voltage through the PE effect. The frequency of these important EM resonances then depends on the effective material parameters and geometry of the PEs.

From the point of view of the constituent phases, large transversal direct voltage ME effects (α_{E3a} , where a and b are the direction indexes equal to 1 or 2) tend to be favored by MS phases with large longitudinal pseudo-piezomagnetic coefficients ($q_{ab} = \partial \lambda_b / \partial H_a$, where λ_b is the H dependent MS strain) and PE phases with a large ratio between transversal piezoelectric (d_{3a}) and longitudinal dielectric constants (ϵ_{33}), as well as an efficient stress transfer between layers [1, 2]. A very promising class of MS materials are the Metglas[®] (Ni-Fe-Mo-B, Fe-Si-B, Co-Fe-Si-Ni-B, etc.) amorphous alloys. This is mainly because of their large piezomagnetic coefficients of $q_{11} \approx 4.0$ ppm/Oe and $q_{12} \approx -2.5$ ppm/Oe [13], very low coercivity and low saturation fields which results in a huge relative magnetic permeability ($\mu_{33} > 10^4$) [7]. As for the PE phase, ferroelectric ceramics of PZT (Pb(Zr,Ti)O₃) have been extensively studied and tend to provide a strong ME coupling due to their relatively large piezoelectric and electromechanical (EM) coupling coefficients [14–16]. Nonetheless, the use of highly anisotropic single-crystalline ferroelectrics, poled and cut along desirable crystallographic directions, constitutes an alternative way to achieve large but also anisotropic ME effects [17, 18]. The current research on ME composites has therefore been remarkably focused on lead-based compounds such as PMN-PT or PZN-PT [1, 3, 19, 20]. Nevertheless, some lead-free PE single-crystals have been recently explored and shown to potentially yield a comparably large direct ME effect in composites. Such systems have included quartz [18], aluminum nitride [17], zinc oxide [21], langatate (La₃Ga_{5.5}Ta_{0.5}O₁₄, LGT) [22, 23] and langasite (La₃Ga_{5.5}SiO₁₄, LGS) [23].

In the present chapter, we report a study of the anisotropic direct ME properties of bulk tri-layered structures of Metglas/LNO/Metglas, Metglas/GPO/Metglas and Metglas/PMN-PT/Metglas using different cuts of the crystalline PEs and under quasi-static and EM resonance conditions.

7.2 Magnetolectric Measurement Techniques

7.2.1 Dynamic Magnetolectric Technique

In general, the experimental measurement of the direct ME effect has proven to be a simpler and more accurate method for the quantification of the ME effect when compared to the measurement of the converse ME effect. The advantages of the first technique include the relative easiness of producing large magnetic fields used to excite the samples and the fact that magnetic fields can generate higher energy densities than electric fields [24]. Also, the possibility of destructive dielectric breakdown, which could be caused by excessively high voltages applied during the measurement of the reverse effect, is avoided. The direct voltage and charge ME effects, quantified by the respective coefficients $\alpha_{Eij} = \partial E_i / \partial H_j$ and $\alpha_{Qij} = \partial D_i / \partial H_j$, with indexes i and j equal to 1, 2 or 3, can be experimentally measured via three fundamental methods [24, 25]:

- (i) The static method, where the sample is subjected to a uniform magnetic bias field (H), and the voltage ($V = E_i \cdot t$, where t is the thickness of the PE phase) or charge ($Q = D_i \cdot A$, where A is the area of the electrodes placed on the PE) developed across its electrodes is measured with an electrometer in voltage (high-input-impedance) or charge (low-input-impedance) mode, respectively. In the charge mode, the input of the electrometer is a virtual ground, and therefore the measurement of charge instead of voltage should be less affected by the problem of leakage currents flowing through the sample due to an eventually small PE conductivity. By applying different magnetic fields, the induced ME voltage can therefore be quantified as a function of H ;
- (ii) The quasi-static method, where a voltage or charge generated across the sample's electrodes is measured using an electrometer as a function of time simultaneously with a slow variation of the applied *DC* magnetic field (with a rate of ca. 0.05–0.5 T/min). Here, the magnetic field is generally increased from zero up to a maximum value, stabilized at this value and subsequently decreased back to zero. A baseline can be subsequently used to correct for an eventual time drift of the voltage/charge due, e.g., to the pyroelectric effect;
- (iii) The dynamic method, where a modulation magnetic field with a frequency f and a small amplitude δH is superimposed on a comparatively large magnetic *DC* bias field H . Using a lock-in amplifier, the *AC* ME voltage generated across the sample or the current flowing through it is then measured as a function of H or f . This dynamic method presents a series of advantages in comparison to the static and quasi-static methods [26, 27]. The first one is a very efficient reduction of the electronic noise thanks to the phase-sensitive detection using a lock-in amplifier. Here, signals with a frequency distinct from the frequency of a reference signal are rejected and filtered by the unit. This method also allows one to eliminate the problem of charge accumulation, observed for certain ceramics, where the charge generated during polarization

of the sample accumulates at its grain boundaries. These charges can move toward the electrodes during the measurements, thus disturbing the experimental results. The relatively high speed of measurement in this method thus allows a minimization of the accumulation of charge. Another advantage is that the ME response may be studied in different modes of operation, e.g., with different values of the magnetic bias field or at different time scales by changing the frequency of the modulation field. However, some negative aspects and special cautions should also be noted. These include [3, 6, 26, 28]: the leakage of charge under periodic conditions, which may occur through the Ohmic resistance of the samples at low frequencies of the AC field, or through the capacitance formed between the two surfaces at higher frequencies. Some parasitic mutual inductance will also exist between the source of the magnetic field and the system composed of the sample and cables connected to its electrodes. A frequency-proportional voltage will therefore always be induced across the electrodes by the applied time-changing magnetic field due to the effect of electromagnetic Faraday induction. Furthermore, we may also have the induction of eddy currents in the system, thus decreasing the effective modulated magnetic field felt by the sample. For high enough frequencies, these effects might even be more significant than the voltage generated by the ME effect in the samples. Some external sources of synchronized noise can also be especially harmful to this technique, including, e.g., the thermal noise, introduced by pyroelectric currents, and, more importantly, external vibrational or acoustic noises (microphony) which can be coupled to the sample via the piezoelectric effect.

In addition to the aforementioned techniques that can be used to measure the direct ME effect, several others have also been tested [25]. Some of those include: (i) active modes of analysis, where a test current is passed through the sample, and subsequently dielectric and polarization measurements are performed in various applied magnetic fields [3]; (ii) techniques using a pulsed magnetic field, which are ideal for the study of EM resonance phenomena [29], and (iii) ME measurements based on the PE effect making use of a microwave microscope or a magnetic cantilever [12].

From this point onwards we will mainly focus on the dynamic lock-in technique since this is the method in which we are most experienced. Thus we begin by presenting a formalism describing this technique and consequently show how the different order ME coefficients can be extracted from the measurements of the voltages synchronized with the fundamental and harmonic frequencies of the magnetic exciting signal. Assuming that the non-linear ME voltage ($V = E \cdot t$) induced across a ME composite as a function of an applied magnetic field (H) can be expanded in a Taylor series centered at a bias field H_0 , it follows that [26]:

$$V(H) = \sum_{n=0}^{\infty} \alpha_n (H - H_0)^n, \text{ with } \alpha_n = \frac{1}{n!} \frac{\partial^n V}{\partial H^n} (H_0). \quad (7.1)$$

When a bias and a modulated AC magnetic field with frequency $f = \omega/2\pi$, given by $H = H_0 + \delta H \cos(\omega t)$ where t stands for time, are applied to this composite, the output voltage thus becomes:

$$V = \sum_{n=0}^{\infty} \alpha_n \cdot \delta H^n \cos(\omega t)^n. \quad (7.2)$$

Next, taking into account that:

$$\cos(\omega t)^n = \begin{cases} \frac{1}{2^{n-1}} \sum_{j=0}^{\frac{n-1}{2}} \binom{n}{j} \cos((n-2j)\omega t), & \text{if } n \in \mathbb{N} \text{ is odd} \\ \frac{1}{2^n} \binom{n}{\frac{n}{2}} + \frac{1}{2^{n-1}} \sum_{j=0}^{\frac{n}{2}-1} \binom{n}{j} \cos((n-2j)\omega t), & \text{if } n \in \mathbb{N} \text{ is even} \end{cases} \quad (7.3)$$

where $\binom{n}{j}$ are the binomial coefficients and substituting this expression in (7.2), one gets:

$$V = \sum_{l=0}^{\infty} \frac{1}{2^{2l}} \binom{2l}{l} \cdot \alpha_{2l} \cdot \delta H^{2l} + \sum_{n=1}^{\infty} \frac{1}{2^{n-1}} \cdot \alpha_n \cdot \delta H^n \sum_{j=0}^{\lfloor \frac{n-1}{2} \rfloor} \binom{n}{j} \cos((n-2j)\omega t), \quad (7.4)$$

where $\lfloor \dots \rfloor$ indicates the nearest lower integer. Introducing the new variable $k = n - 2j$ and changing the order of summation allows us to collect the cosine terms in the last part of the equation:

$$V = \sum_{l=0}^{\infty} \frac{1}{2^{2l}} \binom{2l}{l} \cdot \alpha_{2l} \cdot \delta H^{2l} + \sum_{k=1}^{\infty} \left[\sum_{j=0}^{\infty} \frac{1}{2^{k+2j-1}} \binom{k+2j}{j} \cdot \alpha_{k+2j} \cdot \delta H^{k+2j} \right] \cos(k\omega t), \quad (7.5)$$

which shows that this voltage will be a combination of sinusoidal functions of time with frequencies equal to the frequency of the applied modulation field and its harmonics. The amplitudes associated with each of these harmonic signals will therefore be given by the parameter in brackets:

$$\delta^k V = \sum_{j=0}^{\infty} \frac{1}{2^{k+2j-1}} \binom{k+2j}{j} \cdot \alpha_{k+2j} \cdot \delta H^{k+2j}. \quad (7.6)$$

For example, the amplitudes of the fundamental signal and its first two harmonics are then:

$$\begin{aligned}
\delta^1 V &= \alpha_1 \delta H + \frac{3}{4} \alpha_3 \delta H^3 + \frac{10}{16} \alpha_5 \delta H^5 + \dots; \\
\delta^2 V &= \frac{1}{2} \alpha_2 \delta H^2 + \frac{1}{2} \alpha_4 \delta H^4 + \frac{15}{32} \alpha_6 \delta H^6 + \dots; \\
\delta^3 V &= \frac{1}{4} \alpha_3 \delta H^3 + \frac{5}{16} \alpha_5 \delta H^5 + \frac{21}{64} \alpha_7 \delta H^7 + \dots.
\end{aligned} \tag{7.7}$$

Assuming that the partial derivatives in expansion (7.1) decrease fast enough and δH is sufficiently small, so that $\sum_{j=1}^{\infty} \frac{1}{2^{2j}} \binom{k+2j}{j} \cdot \frac{\alpha_{k+2j}}{\alpha_k} \cdot \delta H^{2j} \ll 1$ for all $k \in \mathbb{N}$, then all higher-order terms in the expansion (7.6) may be neglected, and one can arrive at the commonly made approximation:

$${}^k \alpha_E = \frac{1}{t} \cdot \frac{\partial^k V}{\partial H^k} \simeq 2^{k-1} k! \frac{\delta^k V}{t \cdot \delta H^k}, \tag{7.8}$$

where ${}^k \alpha_E$ is the k -th order H_0 dependent voltage ME coefficient and t is the effective thickness of the PE phase. This expression shows that the amplitude of the k -th harmonic of the voltage ($\delta^k V$) as measured in the lock-in should be approximately proportional to the k -th power of the amplitude of the applied modulation field (δH^k) and to the k -th derivative of the V versus H curve at some bias H_0 field. Therefore we see that in the first order this ratio will be related to the direct voltage ME coefficient through: $\alpha_E = \delta^1 V / (t \cdot \delta H)$.

More generally, to take into account the dispersion and energy losses in the response of the ME coefficients α_n in expansion (7.1) we assume that the output voltage in (7.4) can be described by the convolution relation:

$$V(t) = V_0 + \sum_{k=1}^{\infty} \int_{-\infty}^t \delta^k V(t-t') \cdot \cos(k2\pi f t') dt', \tag{7.9}$$

where t and t' represent the time. Making use of the convolution theorem, the Fourier transform of the above expression will then be:

$$V'(f') = V_0 \delta(f') + \sum_{k=1}^{\infty} \delta^k V'(f') \cdot \frac{1}{2} [\delta(f' - kf) + \delta(f' + kf)], \tag{7.10}$$

where $V'(f')$ and $\delta^k V'(f')$ represent the Fourier transforms of $V(t)$ and $\delta^k V(t)$, respectively, f' the frequency of the output voltage signal, f the frequency of the modulated H field and $\delta(x)$ the Dirac delta function. Therefore, all complex coefficients $\delta^k V'(f')$ in the expansion are now described as functions of the frequency f' . As before, this expression shows that the amplitude of the output voltage signal measured in a lock-in amplifier should only be nonzero at integer multiple frequencies of f . As an example, supposing that all the factors $\delta^k V'(f')$ in this

expression, which depend on the complex ME coefficients ${}^n\alpha'_E(f') = \alpha'_n(f') \cdot n!/t$ corresponding to the Fourier transforms of the ME coefficients ${}^n\alpha_E$ in expression (7.6), given by:

$$\delta^k V'(f', H_0) = \sum_{j=0}^{\infty} \frac{1}{2^{k+2j-1} j! (k+j)!} \cdot t \cdot {}^{k+2j}\alpha'_E(f', H_0) \cdot \delta H^{k+2j}, \quad (7.11)$$

are associated with a ME resonance peak at an arbitrary frequency $f' = f_R$. Then, in the ME measurements (with some constant applied bias H_0) this peak will be observed at $f = f_R$ in the fundamental frequency mode having an amplitude given by $|\delta^1 V'(f_R)| = \sqrt{\delta^1 V'(f_R)^* \cdot \delta^1 V'(f_R)}$. Furthermore, for the 1st and 2nd harmonic frequency detection with $f' = 2f$ and $f' = 3f$, this peak should appear at lower frequencies, $f = f_R/2$ and $f = f_R/3$, with amplitudes $|\delta^2 V'(f_R)|$ and $|\delta^3 V'(f_R)|$, respectively. This last general expression thus allows us to relate the output voltage measured in any detection circuit with the magnetic bias and modulated fields, frequency and characteristic ME voltage coefficient of a particular composite.

7.2.2 Experimental Dynamic Magnetolectric Measurement Setup

As implied in the previous Section, the basic blocks needed to perform dynamic measurements of the direct ME effect are a magnetic field source (usually one or two electromagnets), capable of producing constant and AC magnetic fields which are applied to the sample, and a lock-in amplifier, whose purpose is to measure the AC voltage generated on the sample through the ME effect. Since commercial systems are still unavailable at this point, as an example Fig. 7.1 shows schematically an experimental setup built by our group in order to measure the dynamic direct and converse ME effects [30]. Here, the samples are placed in the center of a plastic box containing a Helmholtz coil capable of generating AC magnetic fields with amplitudes δH of up to 100 Oe as well as constant bias fields H of up to the same value. A DC bias field, in the range of 0–15 kOe, can also be produced by an external electromagnet (Bruker[®] ESP 300E) collinear with the Helmholtz coil and directed along the X direction. This bias field is stabilized by a Hall-sensor-based regulating feedback loop. The Helmholtz coil is driven by a power amplifier (AE Techron[®], model 7224) with a gain between 1 and 20 and low output impedance (28 mOhm in Series with 1 μ H). The current flowing through the coil is stabilized by a current control loop or by taking into account the complex impedance of the whole circuit. The amplitude and frequency of the AC current are set either by an external function generator (SRS[®], model DS345) or by the internal generator of the lock-in amplifier (Zurich Instruments[®], model HF2LI). The AC current passing through the Helmholtz coil is continuously measured by a multimeter (Agilent[®],

model 34401A). The measured current is then used to calculate the previously calibrated magnetic AC field amplitude δH , where a gaussmeter was used, throughout a large frequency range of up to about 600 kHz (for $\delta H = 0.1$ Oe). This current is measured directly, with the multimeter in its ammeter mode, up to a frequency of ca. 10 kHz due to accuracy limitations of the device, and indirectly, with the multimeter in its voltmeter mode, for frequencies larger than 10 kHz by making use of the known complex impedance of the Helmholtz coil or a known reference resistor. A gaussmeter (DSP[®], model 475) is used to measure the exact value of the bias field produced by the external electromagnet. The amplitude and phase of the transverse voltage δV induced across the sample by the applied in-plane AC magnetic field δH is measured with the lock-in. Higher harmonics of the ME signal can also be measured simultaneously in this way by using multiple independent demodulators. The measuring system as a whole can be synchronized by a TTL output signal from the function generator or alternatively by the internal oscillator of the lock-in, depending on the source of the AC signal. The entire setup is autonomously driven by a home-made data acquisition software based on LABview[®]. The direct ME measurements are consequently presented as the direct ME coefficient given by equation $\alpha_E = \partial E / \partial H = \delta V / (t \cdot \delta H)$ as a function of the magnetic bias field H , with an applied constant-frequency modulation field, or as a function of the frequency f of the AC field, with an applied constant bias field. We also point out that, since most lock-in amplifiers have an input impedance of just about between 1 and 10 M Ω , the use of a high input impedance voltage pre-amplifier is usually required in this system, at least at low frequencies (ca. < 10 kHz), in order to achieve the open-circuit condition specified by the definition of the ME voltage coefficient (α_E). Otherwise, the circuit parameters of the sample and measuring device should be taken into account in the calculation of α_E .

Although not optimized for this purpose, we note that this system may also be used to measure the converse ME effect. This measurements are performed by applying an AC voltage (δV_{mod}), produced by a function generator, to the sample and using the Helmholtz coil to pick up the magnetic flux variation due to the changing magnetic permeability of the sample. The amplitude and phase of the voltage induced on the coil (δV_{ind}) as a function of either the driving frequency, at a constant DC magnetic bias field, or of the swept magnetic field, at a constant excitation frequency, are then detected by the lock-in. The resulting ME effect can then be represented as a ratio between the AC voltage detected on the Helmholtz coil and the voltage applied to the sample ($\delta V_{ind} / \delta V_{mod}$) or as the traditionally used converse ME coefficient $\alpha_B = \partial B / \partial E$, in units of G·cm/kV, after properly calibrating the pickup coil. The accessible frequency range for this type of measurements goes from several Hz up to several tens of MHz.

Figure 7.2 displays a picture of the whole setup with its components labeled. A plastic box is used to house the sample and contains the Helmholtz coil which produces the AC magnetic field. It consists of a $60 \times 55 \times 68$ mm³ container built with non-conductive and non-ferromagnetic materials (mostly PVC) close to the coils in order to avoid losses at large frequencies due to eddy currents and a

Fig. 7.2 Photo of the setup used in the ME measurements. The labeled components are:
 1) electromagnet; 2) box containing the Helmholtz coil;
 3) sample support and goniometer; 4) PC; 5) lock-in amplifier;
 6) function generator; 7) multimeter (ammeter/voltmeter); 8) power amplifier;
 9) gaussmeter



concentration of the field lines away from the center of the coil. The two modulation coils are fixed on opposed interior side walls. This box can then be connected to a goniometer and used in sync with a helium flow or a nitrogen flow cryostat, thus allowing measurements from cryogenic temperatures up to about 600 K. The Helmholtz coil scheme was adopted for the modulation because of its simplicity and high uniformity of the generated field in the center of the coils with variations of less than 1 % of its central value inside a central cube with a side length of about $\frac{1}{2}$ the radius of the coil. Both coils were electrically connected in parallel between themselves and into the output of the power amplifier. This type of connection minimizes the equivalent inductance of the coil circuit and thus allows one to produce higher currents with the same voltage for higher frequencies of operation. In order to magnetically calibrate the Helmholtz coil, we calculated and experimentally measured the magnetic field generated in the center of the coil using a gaussmeter, as a linear function of the *DC* driven current, as measured by the ammeter. In order to generate a constant *AC* field over a wide range of frequencies, the complex impedance of the circuit of the Helmholtz coil has to be known. This impedance was measured with the help of the lock-in amplifier. With this information we are thus able to calculate the amplitude of the voltage signal (δv) that has to be applied to the coil at any given frequency (f) in order to generate a desired current amplitude ($\delta i \propto \delta H$) through the simple relation $\delta v / \delta i = \sqrt{R^2 + (2\pi fL)^2}$. All of the aforementioned steps were integrated into the measurement program

written in LabVIEW. We note that, beside the AC field, the Helmholtz coil may also simultaneously be used to produce a bias field of up to 100 Oe, thus allowing direct ME measurements to be performed independently without any external electromagnet.

An important component in this kind of systems is the electrical contact and support for the samples. This support must be able to fix the samples in place while taking into account that a large enough stress applied by the support may negatively affect the sensitive ME effects under resonant conditions. The support must also ensure a good electrical contact to the sample's top and bottom electrode surfaces. The ME voltage signal produced between the electrodes must then be carried by a cable to the input of the lock-in. A very short low-noise coaxial cable or twisted pair cable are ideal in this case. These cables can also be enclosed by a conductive shield thus functioning as triaxial cables where the external conductor provides an electromagnetic shielding of the inner conductors mainly from the AC magnetic field. The voltage difference between the inner conductors of the signal cable can subsequently be measured by the lock-in amplifier operating in differential mode.

There are several issues that should be taken into account in the measurements of the dynamic direct ME effect. One of the most important is the generation of an electromotive force between the electrodes of the sample induced by the time changing AC magnetic flux due to the effect of Faraday induction [3]. This magnetically generated signal, having the same frequency as the modulation field, will thus be detected by the lock-in and can easily pass as a ME signal. From the Faraday law of induction we know that the amplitude of the induced signal is proportional to the amplitude of the modulation field (δB), the area of the "loop" formed by the electrodes and the frequency of the field. It should also be shifted by 90° with respect to the modulated field. Since the phase of an eventual ME signal obtained in the lock-in is generally measured relatively to the phase of the voltage applied to the power amplifier that drives the coil, this fact can be used to our advantage in order to obtain the phase of this ME signal relatively to the modulated field. The expression of the induced electromotive force shows that this effect in principle can be minimized by using relatively small frequencies of operation and reducing the surface area normal to the magnetic field formed between the electric wires (decreasing the amplitude of the modulation field does not help because, as we have seen in (7.8), the amplitude of the ME voltage also tends to be proportional to this value). The effective surface area between wires can be minimized by using coaxial cables or twisted pairs of thin wires or/and by carefully orienting these wires in relation to the applied time-varying magnetic field. Even so, test measurements using a non-ME reference sample with dimensions of approximately $10 \times 10 \times 0.5 \text{ mm}^3$ in our support in the frequency range of up to 600 kHz have shown linear output voltages with slopes of up to ca. $873 \text{ mV}/(\text{Oe} \cdot \text{MHz})$ (see Fig. 7.3a). This value of the induced voltage was obtained for the case of the single-mode detection of the lock-in (i.e. using a simple coaxial cable). On the other hand, in the differential detection mode of the lock-in with the signal being measured between the inner conductors in a triaxial cable, the induced voltage was found to be $467 \text{ mV}/(\text{Oe} \cdot \text{MHz})$. Finally, the use of the lock-in in the differential

detection mode together with a grounded outer thick conductive shield was shown to reduce the Faraday induced voltage in the support by up to ten times down to ca. 81 mV/(Oe·MHz). This is the case because of the ability of the conductive outer tube to effectively shield the interior signal-carrying conductors from the external modulated field. Nonetheless, in most bulk laminate and particulate ME composites this effect is not an issue at low frequencies (up to ca. 1 kHz) because they usually yield ME responses of the order of some tens or hundreds of mV/(cm·Oe) [1, 2, 7, 31, 32]. However, for the case of single-phase multiferroics and thin-film composites this induction can become noteworthy because of the weak nature of the ME coupling. Indeed, in the first case maximum direct ME coefficients of the order of only some mV/(cm·Oe) [32, 33] tend to be observed, while in the second even smaller signals of the order of tens or hundreds of $\mu\text{V}/\text{Oe}$ [3, 33] can be detected due to the small thickness of the thin films (even though the direct coefficients can still be comparable to the ones observed in bulk composites). Also, the eventual generation of eddy currents in the wires may also take an important part in this last case [34]. For samples associated with a weak ME effect a simple method can be used to correct the data from the induction effects. Here, a preceding reference measurement is carried out with a non-ME reference sample with about the same dimensions as the ME sample (e.g. a tri-layered composite of Metglas and Teflon) and using the same parameters as in the subsequent ME measurement. The complex in-phase (X) and out-of-phase (Y) components of the parasitic signal can posteriorly be subtracted from the second ME measurement. An example of this procedure is illustrated in Fig. 7.3b.

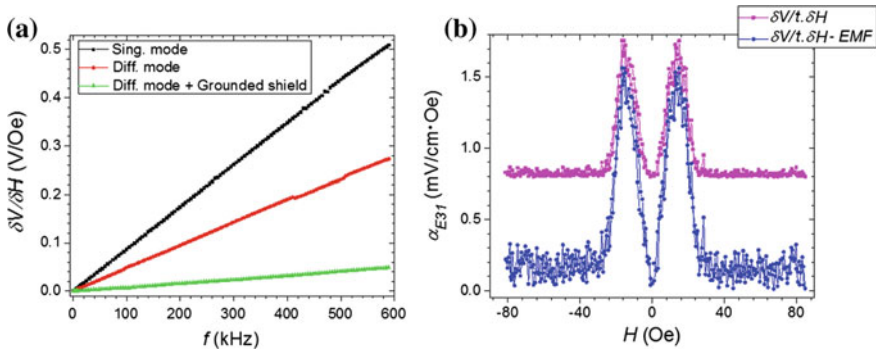


Fig. 7.3 **a** Test dynamic ME measurements performed in a reference non-ME sample while operating the lock-in in its single or differential mode with a grounded or not grounded exterior conductive shield. The observed voltages increase linearly with the frequency of the modulated field ($\delta H = 0.1$ Oe) and are induced between the electrodes by the Faraday effect. **b** Small transversal direct ME effect (α_{E31}) measured in a bi-layered composite of Metglas/Z-cut LiNbO₃ (1 mm thick) with $f = 10$ kHz and $\delta H = 1$ Oe. The originally measured signal $\delta V/t \cdot \delta H$ represents the amplitude of the voltage due to the ME effect superimposed on that generated by the Faraday induction (EMF), of about 0.81 mV/(cm·Oe), which is independent of the bias field. The second curve shows the corrected ME effect obtained by subtracting this second known component

In addition to the electromagnetic induction and intrinsic noise sources such as Johnson, shot and $1/f$ noise, various other extrinsic sources of synchronous noise may negatively influence the results of the experiment. They can be originated, e.g., by capacitive, inductive or resistive coupling between components of the system. The capacitive coupling can be reduced by the use of short cables connected to the samples and by placing such cables far away from eventual sources of stray electric fields (e.g., power amplifiers). Coaxial or twisted cables can be used to minimize the inductive coupling. An electromagnetic shield may also be used to enclose the system containing the sample and Helmholtz coil in order to shield it from stray external DC and time changing electric and magnetic fields. Ground loops can also give rise to a synchronous voltage and are avoided by grounding all of the instruments to the same physical point. Microphonic noise can be minimized by properly fixing the cables and sample support. In our case we also noted the existence of a 50 Hz harmonic noise from the power line, and so measurements at multiple frequencies of 50 Hz were avoided at least up to about 800 Hz, after which this effect is no longer noticeable. The value of the spectral noise density at 1 kHz was estimated as $31 \mu\text{V}_{\text{rms}}/\text{Oe} \cdot \sqrt{\text{Hz}}$, and therefore, in order to obtain a single-to-noise ratio of 100 at 1 kHz with a bandwidth of 1 Hz, a signal of only about 0.44 mV/Oe should be required.

In order to demonstrate the capabilities of this system and the applicability of (7.6) and (7.8), in this part we now present an example of a direct ME measurement performed on a tri-layered composite. In this case, two sheets of the magnetostrictive alloy Metglas were bonded with epoxy to both surfaces of square shaped piezoelectric single crystals of LiNbO_3 . Y- and 41°Y -cut crystals were employed here. Using the setup described above, we first measured the direct ME response of the Y-cut sample as a function of the in-plane magnetic bias field using a modulation field with an amplitude of 1 Oe and a frequency of 1 kHz. The fundamental-frequency voltage signal ($\alpha_{ME1} = \delta V/t \cdot \delta H$), as well as its 1st ($\alpha_{ME2} = \delta^2 V/t \cdot \delta H^2$) and 2nd ($\alpha_{ME3} = \delta^3 V/t \cdot \delta H^3$) harmonics, for $k = 2$ and $k = 3$, respectively, as in (7.8), were measured simultaneously relative to the applied modulated field. These correspond to the component of the generated voltage in phase with the applied modulated field (i.e. the real part of $\delta^k V'(f', H_0)$ as in (7.11)). Figure 7.4 shows the results obtained in this way. The uppermost graph depicts the real part (i.e. in-phase with the modulated field) of the direct ME coefficient (α_{E31}) in units of $\text{mV}/(\text{cm} \cdot \text{Oe})$ as a function of the bias field. Here we can observe that a coefficient as large as $946 \text{ mV}/(\text{cm} \cdot \text{Oe})$ was generated for a field of just about 24 Oe. In general, the shape of the ME curves tend to follow the first derivative of a typical magnetostrictive curve for the Metglas alloy (i.e. $\alpha_{ME1} \simeq \alpha_E = (1/t) \cdot \partial V/\partial H \propto q = \partial \lambda/\partial H$) since the corresponding piezoelectric curve of the PE crystal is highly linear in this range of coupled strains. The second graph, on the other hand, depicts the measured 1st harmonic (at 2 kHz) of the ME output signal in units of $\text{mV}/(\text{cm} \cdot \text{Oe}^2)$. In particular, this signal is shown to be relatively large even for a null bias field. The superimposed red line in this graph

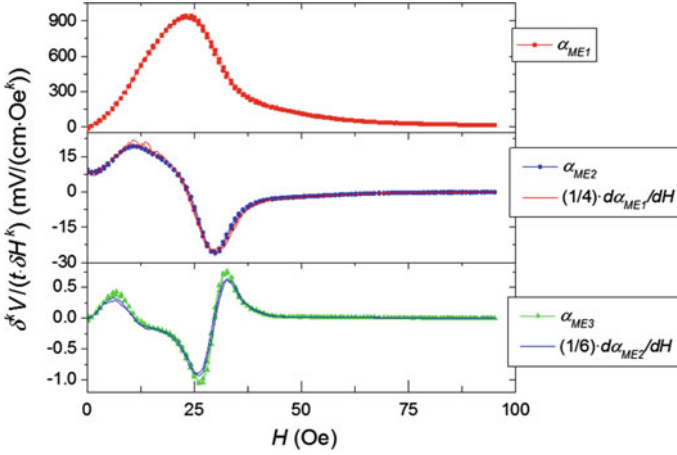


Fig. 7.4 Direct ME effect measurements of a Metglas/Y-cut LiNbO₃/Metglas sample as a function of the bias field at 1 kHz and with $\delta H = 1$ Oe. The uppermost graph shows the ME response detected at its fundamental frequency (α_{ME1}) equal to the frequency of the applied modulated field. The second and third graphs show the 1st (α_{ME2}) and 2nd (α_{ME3}) harmonic response functions, respectively. Superimposed on them are lines representing the numerical derivatives of the previous lower-order harmonic responses

represents 1/4 times the numerical field derivative of the fundamental response in the above graph. This derivative perfectly fits the measured data as predicted by (7.8), where we have: $\alpha_{ME2} = \delta^2 V / t \cdot \delta H^2 \simeq (1 / (4 \cdot t)) \cdot \partial^2 V / \partial H^2 \simeq (1 / 4) \cdot \partial(\delta V / t \cdot \delta H) / \partial H = (1 / 4) \cdot \partial \alpha_{ME1} / \partial H$. The third graph shows the measured 2nd harmonic (at 3 kHz) of the ME response in units of $\text{mV} / (\text{cm} \cdot \text{Oe}^3)$ as a function of the bias field. Superimposed on this response is a line which represents 1/6 times the numerical derivative of the 1st harmonic response. Yet again we see that this derivative fits well the measured signal as predicted by (7.8): $\alpha_{ME3} = \delta^3 V / t \cdot \delta H^3 \simeq (1 / (24 \cdot t)) \cdot \partial^3 V / \partial H^3 \simeq (1 / 6) \cdot \partial(\delta^2 V / t \cdot \delta H^2) / \partial H = (1 / 6) \cdot \partial \alpha_{ME2} / \partial H$. In conclusion, in this measurement we have proven experimentally the validity of (7.8). In practice these ME curves are generally closely related to the non-linear magnetostrictive curves of the MS phase as shown by: $\alpha_{MEk} \simeq (1 / 2^{k-1} k!) \cdot {}^k \alpha_E \propto {}^k q = \partial^k \lambda / \partial H^k$, where ${}^k q$ are the k -th order piezomagnetic coefficients.

The aforementioned setup also allows the measurement of the ME response as a function of the frequency of the modulated field (f) for a fixed bias field. Figure 7.5 shows an example of this measurement for the case of a Metglas/41°Y-cut LiNbO₃/Metglas composite. This measurement was made in the T-L mode (in-plane magnetic field and out-of-plane voltage detection), using a bias field of 25 Oe and a modulated field with an amplitude of 0.1 Oe. The fundamental response (α_{ME1}) as well as its 1st (α_{ME2}) and 2nd (α_{ME3}) harmonics were recorded. In the fundamental mode we note the existence of a single in-plane contour EM resonance mode at a

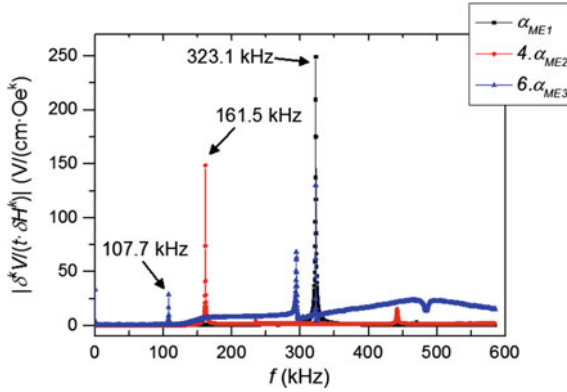


Fig. 7.5 Direct ME effect measurements of a Metglas/41°Y-cut LiNbO₃/Metglas sample as a function of the modulated field frequency with $\delta H = 0.1$ Oe and $H = 25$ Oe. Here, the fundamental frequency detection (α_{ME1}) is plotted in *black*, whereas the 1st ($4 \cdot \alpha_{ME2}$) and 2nd ($6 \cdot \alpha_{ME3}$) harmonic detections are plotted in *red* and *blue*, respectively. The single peak observed in the fundamental mode corresponds to an electromechanical resonance of the composite

frequency of ca. $f_R = 323.1$ kHz. At this frequency, a coefficient as large as 250 V/(cm·Oe) has therefore been measured. As predicted by (7.10), we also see that this same resonance mode is also excited by modulated fields with frequencies of 161.5 kHz ($\simeq f_R/2$) and 107.7 kHz ($\simeq f_R/3$) in the 1st and 2nd harmonic measurements, respectively, through the non-linear MS effect (i.e. $\alpha_{MEk} \propto \partial^k \lambda / \partial H^k$). The amplitudes of these peaks are of approximately 37.1 V/(cm·Oe²) and 4.7 V/(cm·Oe³), respectively. Furthermore, we can also observe the existence of another resonance peak at 323.1 kHz in the 2nd harmonic detection. This resonance peak should correspond obviously to the first harmonic mode of the fundamental contour mode observed at 323.1 kHz, since it is observed at an odd integer multiple of this frequency, and therefore should be strongly excited by a modulated field frequency of 969.3 kHz. This frequency is larger than the maximum modulated field frequency of 600 kHz which can be attained with the equipment due to technical limitations. Thus, we note that higher-harmonic detection can be useful, e.g., in the study of resonance modes of vibration at frequencies larger than the ones which can be achieved in a given Helmholtz coil. The resonance peak observed at 442.3 and 294.7 kHz in the 1st and 2nd harmonic detection, respectively, corresponds to another contour mode of resonance which in the fundamental frequency detection should be observed at ca. 884.4 kHz. In summary, three distinct contour modes of EM resonance of the composite were identified using the aforementioned technique as seen in the 2nd harmonic detection. We finally note that these non-linear resonant ME effects may be found to be very useful in future e.g. for the development of highly sensitive and low-power wideband AC magnetic field sensors [35, 36].

7.3 Experimental Results

7.3.1 Comparative Study of the Direct and Converse Magnetolectric Effects in Tri-Layered Composites of Metglas with LiNbO_3 and PMN-PT Single Crystals

As we noted in the introduction, since the estimated magnitude of the direct ME effect is approximately proportional to the product of the magnetostrictive and piezoelectric properties of the MS and PE phases, carefully engineered composites can in principle exhibit a remarkable ME coupling, orders of magnitude larger than the ones observed in single-phase multiferroics [1, 2]. The same behavior is expected in the case of the converse ME effect. While the former can find applications in the electric detection of magnetic fields [37–39], the latter could be useful in the electrical control of magnetism [40, 41].

For laminated composites operating in the L-T mode, necessary requirements for a large voltage ME effect (α_{E3a}) include a PE phase with large transversal PE coefficients (d_{3a}), small thickness dielectric permittivity (ϵ_{33}^T) and small longitudinal and transversal compliance (s_{ab}^E). Although $\text{Pb}(\text{Zr},\text{Ti})\text{O}_3$ (PZT) ceramics do not satisfy these requirements from a general point of view, the fabrication of PZT-based ME composites is still commonplace [42, 43]. The use of single-crystalline PEs, poled and cut along desirable crystallographic directions, is another possible approach to achieve large ME effects [17, 18, 30]. Among the commercially available single crystals, lead magnesium niobate–lead titanate (PMN-PT) [44] and lead zinc niobate–lead niobate (PZN-PT) exhibit the largest known piezocoefficients and are thus frequently employed in laminate ME structures [19, 20, 39, 45–47]. Nonetheless, both of them are characterized by some notorious drawbacks which include their low Curie and depolarization temperatures (ca. 100 °C), large chemical and electrical instabilities, non-linear hysteretic behavior, uneasy growth of high-quality crystals and consequently a very high price.

Due to these factors, other single crystalline piezoelectrics are being tested at present [17, 18, 21, 22, 30, 48]. Those have included so far lead-free crystals such as barium titanate (BaTiO_3) [49], lithium niobate (LiNbO_3) [30, 50], gallium phosphate (GaPO_4) [51], quartz (SiO_2) [18], aluminum nitride (AlN) [17], zinc oxide (ZnO) [21], langatate ($\text{La}_3\text{Ga}_{5.5}\text{Ta}_{0.5}\text{O}_{14}$, LGT) [22, 23] and langasite ($\text{La}_3\text{Ga}_{5.5}\text{SiO}_{14}$, LGS) [23]. LiNbO_3 (LNO), a uniaxial PE with a very high Curie temperature (~ 1210 °C), in particular could be proven to be a very promising choice. Although the PE coefficients of LNO are up to three orders of magnitude smaller than those of PMN-PT and PZN-PT, its dielectric coefficients also are, and therefore a comparable ME voltage coefficient can be anticipated in composites featuring this compound. Even in the weakly PE quartz [18], the induced ME coefficient has been found to be very large (ca. 175 V/(Oe·cm)) under EM resonance conditions. Optimization of the LNO-based structures is therefore believed to yield comparable or even larger ME coefficients. Among other attractive features of

LNO, one can highlight its relatively low price, high chemical, thermal and mechanical stability, availability of large crystals of high quality and its lead-free nature [30]. Its multifunctionality could also bring new opportunities for devices based on a coupling between optical, magnetic and electric properties. LNO and a closely related PE LiTaO_3 have already been widely used in surface and bulk acoustic wave devices, optical modulators, waveguides, filters, transducers, acoustic microscopes, etc. [52–56]. Experimentally, magnetically tunable surface wave devices were already tested in doped LNO [57, 58]. However, as a PE layer in ME laminate structures, LNO has been considered only in a few studies [50, 59, 60]. A theoretical estimation of the ME effect in a structure of Terfenol/LNO/Terfenol was made in [59] and an experimental study, in [50]. A very significant tunability of the magnetic properties of a polycrystalline nickel film deposited over a LNO single crystal has also been shown [60].

In this section we present a study of the direct and converse ME effects in tri-layered structures of Metglas/LNO/Metglas and Metglas/PMN-PT/Metglas [30]. As the thickness of the MS layer and bonding method were not optimized, those two types of PE crystals were employed in order to perform a comparative study.

In greater experimental detail, several tri-layered ME composites of the 2-2 connectivity type were fabricated by bonding thin foils of the amorphous Metglas (Ni-Fe-Mo-B) MS alloy to opposite sides of square shaped $10 \times 10 \times 0.5 \text{ mm}^3$ PE single crystals of LNO and PMN-31 %PT poled in the [011] direction. Commercially available 29 μm thick sheets of 2826 MB type Metglas[®] (Hitachi Metals Europe GmbH) were cemented to opposite surfaces of LNO single-crystals (Roditi International Corporation Ltd.) and PMN-PT (H.C. Materials Corp.) using a commercial cyanoacrylate-based glue. Both PE crystals were poled by the suppliers after growth. In this study we used Y-cut and 41°Y-cut crystals of LNO. The LNO crystal has a trigonal symmetry (belonging to the point group $3m$), and its polarization vector lies along the c-axis. The corresponding anisotropic PE, dielectric and elastic constants of the substrates can be calculated by rotating the crystallographic frame of the system, for which the coefficients can be obtained from the literature [61], with respect to their respective laminate frames [59]. The in-plane PE coefficients of the Y-cut LNO substrate were therefore calculated as $d_{31} = -20.8 \text{ pC/N}$ and $d_{32} = 0$, while an out-of-plane dielectric constant of $\epsilon_{r33}^T = 85.2$ was obtained. On the other hand, the 41°Y-cut crystal has PE constants $d_{31} = -16.3 \text{ pC/N}$ and $d_{32} = -17.5 \text{ pC/N}$ and a relative permeability of $\epsilon_{r33}^T = 60.9$. The PMN-PT crystals used were poled along their thickness direction (i.e. along [011]), so that a $mm2$ multidomain symmetry was engineered [44, 62] with effective in-plane extensional PE constants $d_{31} \approx -1750 \text{ pC/N}$ and $d_{32} \approx 564 \text{ pC/N}$ and relative dielectric out-of-plane constant of $\epsilon_{r33}^T \approx 4600$ [44, 62].

In order to study the EM and ME properties of the samples, impedance spectroscopy, as well as direct and converse ME effect measurements were carried out. The impedance measurements were performed in the frequency range of 10 Hz–10 MHz. In this case a simple I-V circuit was used with a reference resistor connected in series with the piezocrystal, with gold electrodes deposited on each

surface, and the frequency of a constant voltage signal generated by an internal source of the lock-in was swept. The amplitudes and phases of the voltage developed across the reference resistor were then detected by the lock-in amplifier, and, using a simple equivalent circuit model, the active and reactive parts of the sample impedance were subsequently obtained. The whole measuring procedure was controlled by a home-made LabVIEW[®] based program. This technique was used mainly in order to determine the quasi-static dielectric constant of the tri-layers and observe their characteristic EM resonances.

The results of the impedance measurements are shown in Fig. 7.6 in the form of the absolute admittance, $|Y|$, as a function of the frequency. Here we can distinguish a series of characteristic EM resonance and anti-resonance peaks. The sound velocity for longitudinal waves in LiNbO₃ propagating along the principal axes is: for the Z direction, 7.271×10^5 cm/s; for the Y direction, 6.549×10^5 cm/s; and for the X direction, 6.580×10^5 cm/s [61, 63, 64]. Applying these values to the case of

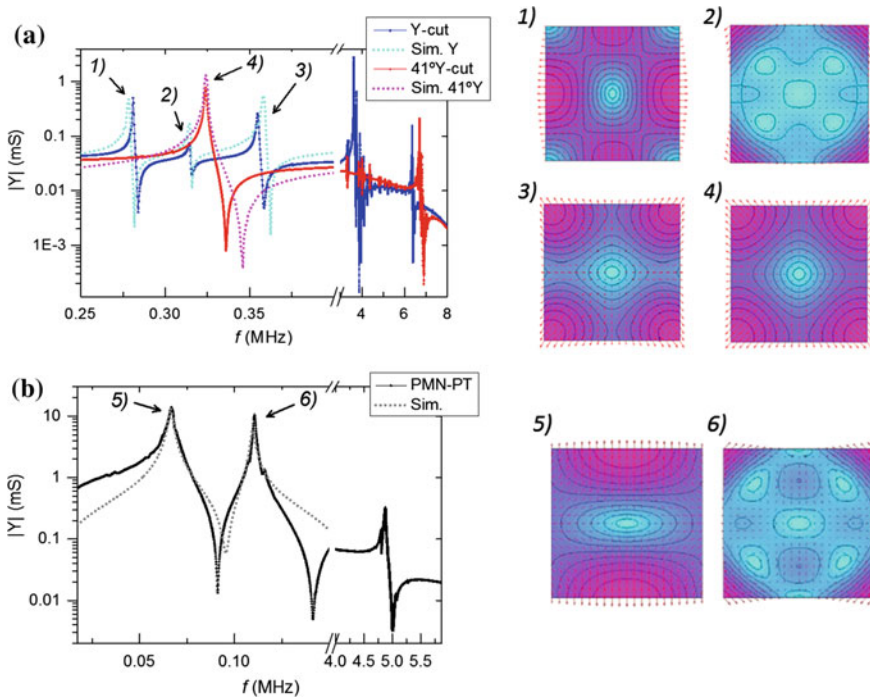


Fig. 7.6 On the left experimental and simulated impedance spectra of **a** LNO and **b** [011]-poled PMN-PT PE single crystals depicting its various characteristic EM resonance ($|Y| \rightarrow \infty$) and anti-resonance ($|Y| \rightarrow 0$) modes. On the right spatial distribution of the in-plane relative displacement fields associated with each type of observed contour EM resonance mode labeled as (1)–(6). Here, more purple regions correspond to larger relative displacement amplitudes while more cyan regions are associated with small displacements. The superimposed small red arrows depict the direction of such displacements [30]

a $10 \times 10 \times 0.5 \text{ mm}^3$ Y-cut LNO crystal, we see that the thickness extensional mode should roughly appear at ca. 6.58 MHz. The closest observed peak is centered at a slightly lower frequency of 6.34 MHz. The calculated length extensional resonances along the X and Z directions (327.5 and 363.5 kHz, respectively) can be associated with the peaks observed at 281, 314 and 355 kHz. The remaining peak centered at 3.65 MHz should be attributed to a shear thickness mode. This mode could be mediated by the relatively large d_{34} coefficient (-69.2 pC/N). In the case of the 41°Y -cut LNO crystal, the thickness shear mode is much less intense because of a much smaller $d_{34} = 3.83 \text{ pC/N}$ [63, 64]. Also, in this case the two largest peaks observed at 323.9 kHz and 6.71 MHz must correspond to contour and thickness modes of vibration, respectively.

In order to exactly identify the in-plane contour acoustic vibrational modes of the LNO crystals observed in the impedance measurements, we implemented a simple model capable of predicting the dynamic electrical behavior of the crystals. More precisely, we numerically solved the thickness-averaged linear elastic and quasi-electrostatic equations of the crystals using a two-dimensional finite element-method (FEM). In the two-dimensional approximation [65, 66], where the thickness of the crystal is assumed to be much smaller than its length, we end up with a system of partial differential equations (PDEs) that can be solved numerically after prescribing the elastic displacements or stresses and electric potentials or electric displacements on the boundary surfaces of the media (i.e. the boundary conditions). Setting the appropriate material constants for each orientation of the crystal and assuming a grounded bottom electrode and a harmonic homogenous potential on the upper electrode ($\delta V_3 e^{j\omega t}$), as well as a null electric displacement field normal to the side surfaces and a null traction over all boundaries, the admittance at each frequency was calculated. To do this, the current flowing through a transverse section of the crystal was obtained by integrating the time derivative of the harmonic displacement field over this surface (i.e. $\delta I_3 = j\omega \int_{Area} \delta D_3 dA$).

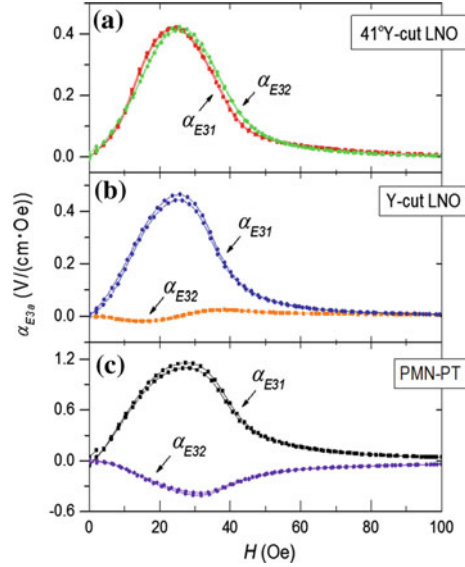
The results of these simulations for the Y-cut and 41°Y -cut crystals are plotted in Fig. 7.6a along with the experimental data. Here we observe a good agreement between the simulated and experimental results and can perfectly identify a correspondence between the resonance and anti-resonance peaks in each type of Y-cut crystal. Therefore, we confirm the existence of three contour modes of resonance in the Y-cut crystal, situated at approximately 278, 314 and 358 kHz, and a single mode for the 41°Y -cut crystals at ca. 324 kHz. By setting the frequency of the applied voltage in the model to a value corresponding to some characteristic resonance mode and plotting the amplitude of the spatial distribution of the in-plane displacement fields, we can analyze and identify the contour resonance modes associated with each peak. The modes thus found are labeled and represented in Fig. 7.6a which shows the absolute value of the displacements along the plane of the PE in a color scale (from blue for a null displacement to pink for large displacements) and the directions of these displacements as red arrows. Thus, the three resonance modes observed in the Y-cut crystal correspond to the three contour

acoustic modes labeled as: (1), (2) and (3). All of those are non-trivial modes because of the relatively complex geometry of the system. The mode (1) is comparable to an extensional mode of type I, as labeled by the IRE standard [67], just like the mode (3). In summary, the mode (1) is characterized by oscillatory displacements mainly along the central region of each face, while the central and vertex regions stay almost still. In mode (2) there is a periodic bending of the vertexes to the sides. The (3) mode is associated with a periodic displacement of the vertex regions of the plane along the radial direction. Since the (1) and (3) modes are associated with larger displacements over larger areas, they naturally produce larger variations of the current flowing through the crystals and consequently larger resonant peaks. The single large resonant mode observed in the 41°Y -cut crystal labeled (4), on the other hand, corresponds to a symmetric contour mode of the type III [67] where the crystal periodically expands and contracts almost isotropically in both in-plane directions and is generated due to the almost in-plane isotropic nature of the material constants in this case.

For the case of the PMN-PT based tri-layer, two low-frequency modes (67 and 111 kHz) and one high-frequency mode (4.87 MHz) are observed, as shown in Fig. 7.6b. According to [68], the sound velocity for the longitudinal mode propagating along the Z direction is 4.727 cm/s, which yields for a thickness extensional resonance a frequency of about 4.73 MHz that is close to the experimentally observed value. Using the same model as in the aforementioned case, we identified the contour resonance modes responsible for the two observed low-frequency peaks. Those are labeled (5) and (6) and are shown in Fig. 7.6b. The first of these modes therefore corresponds to a simple extensional mode, while the second exhibits a behavior similar to the one observed in the mode (2). When compared to the electrically excited contour resonant modes of the LNO crystals, the resonant admittance peaks measured in the PMN-PT crystal are shown to be one order of magnitude larger, which should be a result of a much stronger PE effect in this crystal.

Measurements of the direct ME effect were carried out at room temperature and at a frequency of 5 kHz in the quasi-static regime, i.e. far enough from any observed EM resonances. The modulation amplitude of the AC field was fixed at $\delta H = 1$ Oe, while the transversal ME voltage coefficients α_{E31} and α_{E32} (given by (7.8) for $k = 1$) were measured in two orthogonal in-plane orientations. Thus, α_{E31} was measured with the bias field H oriented along the X direction in the laminate frame, while α_{E32} was measured with H oriented along the Y direction. Figure 7.7 shows the experimental results obtained. In the general case we start by noting that the soft magnetic properties of the Metglas alloy are responsible for the appearance of the maximum ME effect in magnetic fields as low as 25 Oe. The region where the ME effect is not null corresponds to the field range where the magnetization vector of the MS phase increases by the rotation of magnetic domains and by domain wall motion. The saturation of the ferromagnetic foil occurs at $H \approx 50$ Oe, after which any further increase of the external bias field does not lead to any substantial increase of the strain in the thin foil (i.e. the magnetostriction attains its saturation value λ_S), and consequently the ME effect vanishes. Furthermore, as it was

Fig. 7.7 Direct voltage ME effects measured in the tri-layered composites of Metglas/PE/Metglas with PE single-crystals of **a** 41°Y-cut LNO; **b** Y-cut LNO and **c** [011]-poled PMN-PT (with $f = 5$ kHz and $\delta H = 1$ Oe) [30]



expected, we see that the samples demonstrate an anisotropy of their in-plane ME properties due to the anisotropy of the PE properties. The sample containing the Y-cut LNO crystal exhibits a difference between α_{E31} and α_{E32} of more than an order of magnitude. The respective measured values were $\alpha_{E31} = 0.46$ V/(cm·Oe) and $\alpha_{E32} = 0.024$ V/(cm·Oe). In this crystal we have $d_{31} = -20.8$ pC/N and $d_{32} = 0$ and, consequently, the small observed α_{E32} coefficient is exclusively generated by the transversal Poisson stress of the magnetostriction acting on the d_{31} component. In the latter case, the magnitude of the ME induced voltage was comparable to the parasitic electromagnetic induction voltage, so that the corresponding correction has been applied. On the other hand, in the 41°Y-cut LNO crystal sample an almost isotropic in-plane behavior has been observed with $\alpha_{E31} \approx \alpha_{E32} \approx 0.42$ V/(cm·Oe), which is due to almost equivalent values of the d_{31} and d_{32} piezocoefficients (-16.3 pC/N and -17.5 pC/N, respectively). For the case of the PMN-PT composite, the d_{31} piezoconstant is twice as large as d_{32} and has a different sign. As a result, the maximum of α_{E31} corresponds to 1.15 V/(cm·Oe), while the maximal amplitude of α_{E32} equals -0.41 V/(cm·Oe). Following the procedure described in [59] and using the Metglas and PMN-PT material parameters measured by the suppliers and by independent sources [44, 62], we calculated the maximum expected quasi-static values of α_{E31} and α_{E32} for our specific sample to be $\alpha_{E31} = 23.2$ V/(cm·Oe) and $\alpha_{E32} = -7.2$ V/(cm·Oe). These values are more than one order of magnitude larger than the experimental ones. This may be mainly due to a weak coupling between interfaces, where the intermediate glue layers absorb part of the tensile stress being transferred from the MS to the PE phase, and a non-optimized PE/MS thickness ratio between phases, where composites with much thicker MS phases are expected to generate considerably larger effects due to a minimal compressive stress

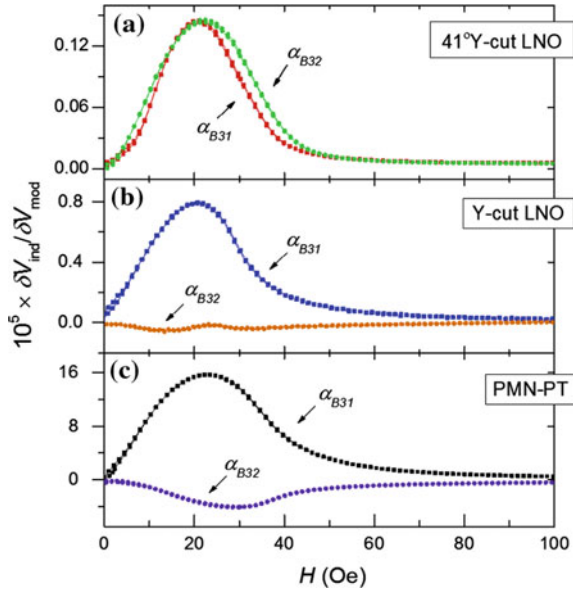
produced by the thin PE substrate on the MS phases [69]. Nevertheless, as both of these factors should result in an identical reduction of the ME effect in the PMN-PT and LNO based composites, further discussion shall be more focused on the relation between the measured coefficients rather their absolute values.

A very important point can be drawn from the quasi-static direct ME measurements. The maximum amplitudes of the observed ME voltage coefficients for the LNO tri-layers are only about three times lower than those for the PMN-PT composite. The maximal ME voltage coefficient for the PMN-PT tri-layer is 1.16 V/(cm·Oe), while for the LNO tri-layers employing Y-cut and 41°Y-cut crystals it is 0.47 and 0.42 V/(cm·Oe), respectively. Comparable magnitudes are mainly explained by the fact that the dielectric constant of PMN-PT is more than 60 times larger than that of LNO. Consequently, the same amount of charge generated by piezoelectricity gives rise to a 60 times lower voltage in PMN-PT. Therefore, the huge piezoelectric coefficients of PMN-PT are effectively nullified by its also huge dielectric coefficients in terms of the open-circuit ME effect.

As we have seen, the magnitude of the direct ME voltage coefficient can be comparable in LNO- and PMN-PT-based composites because this response is approximately proportional to the ratio between the PE coefficients and dielectric constants. However, this concurrent influence on the composite's performance is no longer favorable for the case of the converse ME effect because this effect is independent of the dielectric constants [70–73]. Thus, in this regime, the huge difference in piezoelectric coefficients between PMN-PT and LNO becomes crucial, and the PMN-PT composites should exhibit much stronger converse ME responses. To show this, we performed converse ME measurements on the three composites. Figure 7.8 shows the converse magnetoelectric response represented as the ratio between the electromotive force induced on the sensing Helmholtz coil, δV_{ind} , and the voltage applied to the tri-layered composite, $\delta V_{mod} = 10$ V. This effect is associated with a change in the effective permeability of Metglas when under a stress, which is transferred from the PE substrate. As expected, the dependences of the converse ME effect as a function of the external magnetic bias field are shown to be qualitatively similar to those observed in the direct ME effect measurements, diverging between the different composites only in terms of amplitude. In fact, the composite with the 41°Y-cut LNO exhibits a two orders of magnitude lower response than the one with PMN-PT. Beyond any doubt, the large difference between PE coefficients becomes crucial in this mode. In conclusion, even though the direct ME voltage response is comparable in both composites, the benefits of using PMN-PT crystal for the converse ME effect as well as the direct short-circuit ME charge response in such laminate structures remains indisputable.

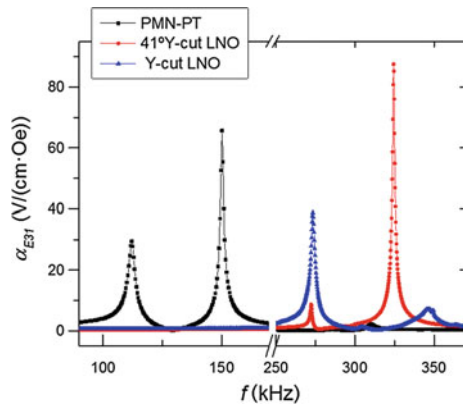
Returning to the direct ME effect measurements, the benefits of PMN-PT already do not look so convincing. The three times greater ME voltage coefficient hardly seems to justify an order of magnitude higher price and lower Curie temperature of the PMN-PT crystal. When measured as a function of the AC magnetic field frequency, f , the EM resonance modes observed in the impedance measurements can also be detected in the direct ME effect. These measurements were performed in the range of 20 Hz–600 kHz (with a fixed bias field $H = 25 - 30$ Oe and an AC field

Fig. 7.8 Converse ME effects measured (given by the ratio between the voltage induced in the sensing coil, δV_{ind} , and the voltage applied to the composites, $\delta V_{mod} = 10$ V) in the tri-layered composites of Metglas/PE/Metglas with PE single-crystals of **a** 41°Y-cut LNO; **b** Y-cut LNO and **c** [011]-poled PMN-PT [30]



amplitude $\delta H = 0.5$ Oe). The results depicted in Fig. 7.9 show the characteristic large increase in the direct response of the composites under such resonance conditions (more precisely the impedance anti-resonance conditions). Surprisingly, the system with the 41°Y-cut LNO crystal yielded the largest effect of ca. 88 V/(cm·Oe) at the largely symmetric resonant mode (4) shown in Fig. 7.6, while in the PMN-PT system the maximum was only of 66 V/(cm·Oe). We also note that the EM resonance is situated in a very suitable frequency range. From the point of view of possible sensor applications, a full implementation could be done using standard low-cost electronic components.

Fig. 7.9 Direct transversal ME effects (α_{E31}) measured in the tri-layered Metglas/PE/Metglas composites as a function of the modulated field frequency f with $H = 25$ Oe and $\delta H = 0.5$ Oe [30]



In summary, in this part we presented a study of the ME and EM properties of 2-2 type Metglass/LiNbO₃/Metglas and Metglas/PMN-PT/Metglas tri-layers using single-crystalline substrates with different cuts. Due to the simplified preparation method, the amplitude of the observed ME effect was rather modest. In qualitative terms, although the highly piezoelectric PMN-PT-based composite has exhibited an orders of magnitude stronger converse ME effect, the measurements of the direct ME effect have shown comparable magnitudes for both types of systems, mainly due to the much higher dielectric constant of PMN-PT. At EM resonance, the largest direct ME voltage coefficient of about 88 V/(cm·Oe) has been obtained for the 41°Y-cut LNO composite, while the second largest coefficient of 66 V/(cm·Oe) was observed for the PMN-PT-based structure. Therefore, in this study we identified crystalline LNO as a valuable alternative to lead-based PEs in ME applications with the potential to form its own field of ME-based low-cost high-temperature magnetic-field sensors.

7.3.2 Comparison of the Anisotropic Magnetoelectric Effects in Tri-Layered Composites of Metglas with LiNbO₃ and GaPO₄ Single Crystals

In the previous section we showed how the use of highly anisotropic single crystalline LNO in ME tri-layered composites can yield very remarkable quasi-static and resonant ME effects. Besides LNO, a noteworthy piezocrystal for ME applications is gallium orthophosphate (GaPO₄, GPO) a commercially available piezoelectric crystal with a trigonal structure (point group 32) and excellent high-temperature properties [74]. As a crystal homeotypic to quartz, it possesses many properties similar to the latter. Characteristic of this material are its larger piezoelectric coefficients when compared to quartz (ca. 1.2 times larger e_{11} and 2.5 times larger e_{14}) [74]. Other desirable properties of the compound are its high thermal stability, with its piezoelectric coefficients and most of its properties barely changing up to a cristobalite transition at 933 °C, large ratio between PE and dielectric constants (d_{3a}/ϵ_{33}), the absence of ferroelectricity and pyroelectricity, a higher EM coupling as compared to quartz, and a high purity of the as-grown crystals [74, 75]. In the present part, we report a study of the anisotropic direct ME properties of enhanced bulk tri-layered composites of Metglas/LNO/Metglas and Metglas/GPO/Metglas, making use of differently oriented crystalline PEs and under quasi-static and EM resonance conditions [76]. The maximum expected quasi-static ME coefficients in each case were numerically estimated as a function of the crystal orientation and compared with the experimental results. The physical origin of the in-plane directional ME response was therefore uncovered.

In order to numerically investigate the nature of the anisotropic ME coupling in tri-layered composites of amorphous Metglas and piezocrystals of LNO and GPO, the maximum direct transversal ME voltage coefficients, $\alpha_{E3a} = \partial E_3 / \partial H_a$, were

numerically estimated for a series of such structures. A standard averaging linear quasi-static micromechanical method based on coupled constitutive equations for each layer was used for this purpose [59, 69]. Here, a square shaped $10 \times 10 \text{ mm}^2$ ME tri-layered structure composed of two $29 \text{ }\mu\text{m}$ thick foils of Metglas and one central 0.5 mm thick piezoelectric crystal, operating in the L-T mode, like the one shown in Fig. 7.1, was considered. Its constitutive elastostatic, electrostatic and magnetostatic equations were then solved assuming averaged homogeneous tensor fields in each perfectly elastically coupled layer ($k_C = 1$) and under unclamped and open circuit boundary conditions. The required linear anisotropic electric, magnetic and elastic material constants were obtained from the literature (Metglas [77–79], LNO [61], and α -GPO [74, 75]). We note at this point that a pseudo-piezomagnetic approximation was assumed for the MS layer which is valid in the small region of the magnetostriction curve where the elastic strain (S_i) changes linearly with the applied bias field (H_k), and the slope $\partial S_i / \partial H_k$ is maximized so that $S_i = q_{ki} H_k$ where q_{ki} describes the piezomagnetic coefficient. In the case of a traction-free Metglas layer the $\partial S_i / \partial H_k$ slope takes a maximum value of ca. 4 ppm/Oe for a bias field of ca. 10 Oe, which was therefore used as our q_{11} coefficient [80].

Since the material properties of single crystals are highly anisotropic, the optimization of the piezocrystal orientation (crystal-cut) can in principle lead to significantly enhanced ME coefficients in composites. To investigate the dependence of the maximum ME coupling coefficient with the crystal orientation, the material tensors were transformed from the crystalline frame to the frame of the laminate using the classic Euler angles $Z_1 X_2 Z_3$ corresponding to a sequence of three rotations each denoted by the angles α , β and γ [59, 62, 81]. The results obtained in this way are shown in Fig. 7.10 as representation surfaces of $|\alpha_{E3a}|$ maximized in the range of all γ angles between 0° and 180° and as a function of the α and β angles for the

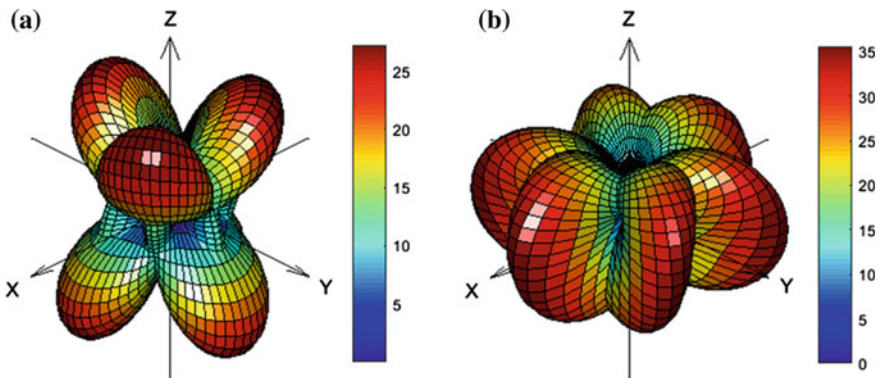


Fig. 7.10 Representation surfaces depicting the maximum estimated absolute values of the transversal ME voltage coefficient $|\alpha_{E3a}|$ (across $0 < \gamma < 180^\circ$) as a function of the crystal orientation (normal to the plane of the laminate associated with the rotation angles α and β) for the tri-layered ME composites of Metglas/Piezocrystal/Metglas, whit piezocrystals of: **a** LiNbO_3 ; and **b** $\alpha\text{-GaPO}_4$

composites containing LNO and GPO. A very large variation of the magnitude of the transversal ME effect with the orientation of the piezocrystal, whose symmetry coincides with the symmetry of the corresponding crystal's point group, can be observed. As strong ME effects are particularly important in applications requiring high efficiencies and sensitivities, we conclude that the selection of a crystal with an appropriate cut is a very important step in the development of ME sensors. For the case of the LNO crystal, we see that the calculated ME coefficient could potentially be as large as 27.24 V/(cm·Oe) for a crystal with a (ZXL) 39°-cut ($\alpha = 0^\circ$, $\beta = 39^\circ$ and $\gamma = 90^\circ$) and five other cuts equivalent by symmetry. In commercially available crystals this orientation is commonly denoted as 129°Y-cut. An even larger maximum coefficient of 35.62 V/(cm·Oe) was predicted for the GPO crystal with a (XYI) 12°-cut ($\alpha = 90^\circ$, $\beta = 90^\circ$ and $\gamma = 12^\circ$) and five other equivalent orientations. This cut is very close to the commonly available X-cut crystals ($\alpha = 90^\circ$, $\beta = 90^\circ$ and $\gamma = 0^\circ$).

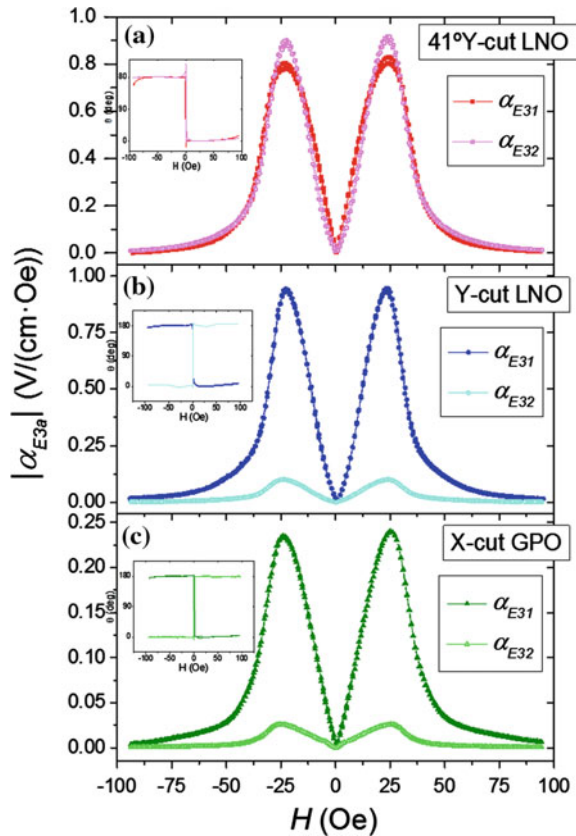
For comparison we also used the model described above in order to calculate the transversal ME coefficients for the particular case of the piezocrystals employed in the experimental part. Those consisted of Y-cut ($\alpha = 0^\circ$, $\beta = -90^\circ$ and $\gamma = 0^\circ$) and 41°Y-cut ($\alpha = 0^\circ$, $\beta = -49^\circ$ and $\gamma = 0^\circ$) LNO as well as X-cut ($\alpha = 90^\circ$, $\beta = 90^\circ$ and $\gamma = 0^\circ$) GPO. The results thus obtained indicate, for the 41°Y-cut crystal, maximum values of α_{E31} and α_{E32} in-phase and with approximately the same magnitude ($\alpha_{E31} = 11.2$ V/(cm·Oe) and $\alpha_{E32} = 11.9$ V/(cm·Oe)), which is due to almost equivalent d_{31} and d_{32} PE coefficients (-16.5 pC/N and -17.5 pC/N, respectively). In the composite containing the Y-cut crystal, on the other hand, there should be a very large anisotropy in its transversal ME effect ($\alpha_{E31} = 11.6$ V/(cm·Oe) and $\alpha_{E32} = -1.3$ V/(cm·Oe)). This is the case because the transversal piezoelectric coefficients are very different: $d_{31} = -20.8$ pC/N and $d_{32} = 0$. Consequently, the small α_{E32} coefficient is generated only by the traction component perpendicular to the magnetic field, which originates from the Poisson effect, acting on the d_{31} PE component. In the system with X-cut GPO a behavior similar to the aforementioned one was also predicted ($\alpha_{E31} = 34.0$ V/(cm·Oe) and $\alpha_{E32} = -3.8$ V/(cm·Oe)), since the PE constants are similarly given by $d_{31} = -4.37$ pC/N and $d_{32} = 0$.

Subsequently, to experimentally investigate the direct ME effect we prepared tri-layered structure containing two 29 μm layers of 2826 MB Metglas (Hitachi Metals Europe GmbH) bonded on both faces of $10 \times 10 \times 0.5$ mm³ square-shaped commercial PE single crystals of congruent LNO and GPO (Roditi International Corporation Ltd.) cut along desirable crystallographic directions. These consisted of substrates of Y-cut, 41°Y-cut LNO and X-cut GPO (Roditi International Corporation Ltd.) bounded to Metglas using a commercial epoxy resin which was cured for 24 h. This type of adhesive is commonly used in the preparation of ME layered composites [1–5, 7, 12, 31, 33, 82] and is well known for its good mechanical, thermal and chemical properties. Their anisotropic ME and EM properties were subsequently studied.

Using the setup described in Sect. 2.2, we measured the direct ME effect in the quasi-static regime in each of the three composites. The tri-layered structures were subjected to a fixed AC magnetic field with amplitude $\delta H = 1$ Oe and a frequency of

1 kHz. The magnetic bias field H was then applied in the X and Y directions in relation to the samples and swept in such a way so as to measure the hysteretic in-plane α_{E31} and α_{E32} ME coefficients (i.e., with the field increasing from zero up to its maximum value followed by a decrease down to a minimum value and an increase back to zero). The results of these measurements are plotted in Fig. 7.11. As in the previous comparative study, we see that the maxima of the ME effects are attained at magnetic fields as low as 25 Oe, which is due to the soft magnetic properties of Metglas. We also note an almost complete absence of a hysteretic response, which confirms the linear nature of the piezoelectric properties of both LNO and GPO. An imperative observation is that, as expected, all of the samples exhibit a significant anisotropy of their in-plane ME properties ($\alpha_{E31} \neq \alpha_{E32}$). Such noticeable differences are mostly related to the anisotropic nature of the material constants of the piezocrystals, mainly their piezoelectric d_{3a} coefficients. In the case of the tri-layered composite with the 41°Y-cut LNO crystal, maximum effects of $\alpha_{E31} = 0.83$ V/(cm·Oe) and $\alpha_{E32} = 0.92$ V/(cm·Oe) were obtained. This response corresponds to an almost isotropic in-plane ME behavior with $\alpha_{E32} \approx \alpha_{E31}$ in agreement with the predictions made in the preliminary calculations. This behavior

Fig. 7.11 Direct quasi-static transversal ME effect measurements ($|\alpha_{E31}|$ and $|\alpha_{E32}|$) of the tri-layered composites of Metglas and a 41°Y-cut LNO, **b** Y-cut LNO, or **c** X-cut GPO, with $f = 1$ kHz and $\delta H = 1$ Oe [76]. The insets depict the phase (in degrees) corresponding to each ME coefficient



contrasts with the structure containing the Y-cut LNO crystal which exhibits a difference between maximum absolute values of α_{E31} and α_{E32} by almost an order of magnitude. This is the case because the d_{32} PE coefficient happens to be null in this orientation. The obtained values here were $\alpha_{E31} = 0.95 \text{ V}/(\text{cm}\cdot\text{Oe})$ and $\alpha_{E32} = -0.10 \text{ V}/(\text{cm}\cdot\text{Oe})$. We also note that both maximum coefficients have a different sign. The positive value defines an in-phase dependence between the applied AC magnetic field and the induced AC voltage and the negative value indicates an out-of-phase relation between these fields. Finally, we see that the sample with the X-cut GPO piezocrystal equivalently yields an almost anisotropic unipolar response with maximum ME coefficients of $\alpha_{E31} = 0.24 \text{ V}/(\text{cm}\cdot\text{Oe})$ and $\alpha_{E32} = -0.03 \text{ V}/(\text{cm}\cdot\text{Oe})$, as was already predicted by our calculations.

Considering again the preliminary calculations, we conclude that all of the experimental results are in a good qualitative agreement with the theoretically estimated effects. However, in quantitative terms, the obtained coefficients were still one order of magnitude smaller than the maximum calculated ones. The main reasons for this should be attributed to a far from optimal thickness ratio between the PE and MS phases and elastic coupling between phases. Additionally, because the magnetostrictive response of the MS alloy is highly non-linear, its pseudo-piezomagnetic q_{ki} coefficients change abruptly with the bias field and stress tensor. In fact, a more sophisticated model for the MS phase [83] shows that the large compressive pre-stress produced by the thick PE in the direction of the applied bias field tends to decrease the maximum value of q_{ki} and increase the bias field at which it is attained. Also, our calculations predicted a three times larger effect in the system with GPO in relation to the one with Y-cut LNO. Since all samples were prepared in the same manner, this seems to be in disagreement with the experiment. A likely explanation is the existence of a large discrepancy between piezoelectric and dielectric coefficients of GPO as the ones found in the literature due to variations in the growth and poling techniques [74, 75, 84]. It may also be related to limitations of the model which, e.g., does not take into account possible stress relaxation occurring along the thickness of the piezoelectric layer nor the properties of the interfaces between the piezoelectric crystals and the layers of epoxy with a finite thickness.

To investigate the dynamic properties of the composites we again started by performing impedance measurements of the PE crystals alone. Figure 7.12 shows the results thus obtained in the form of a) the absolute impedance $|Z|$, as a function of the frequency and (b) the corresponding Nyquist plots of the impedance ($-Z''$ vs Z' , where Z' is the real and Z'' the imaginary parts of Z , respectively). These figures clearly illustrate a multitude of EM resonances (where $|Z|$ attains a minimum value) and anti-resonances (where $|Z|$ attains a maximum value) in the frequency range between 150 and 390 kHz. The amplitude and frequency of the anti-resonance modes is particularly interesting because, as we shall see later, these modes are strongly linked with the resonant peaks observed in the dynamic ME measurements. Of notice is the fact that the X-cut GPO crystal was shown to produce four different resonant modes which are nonetheless much weaker than those found in the LNO substrates and appear at smaller frequencies, due to ca. 3 times larger compliance coefficients in the former [61, 74, 75].

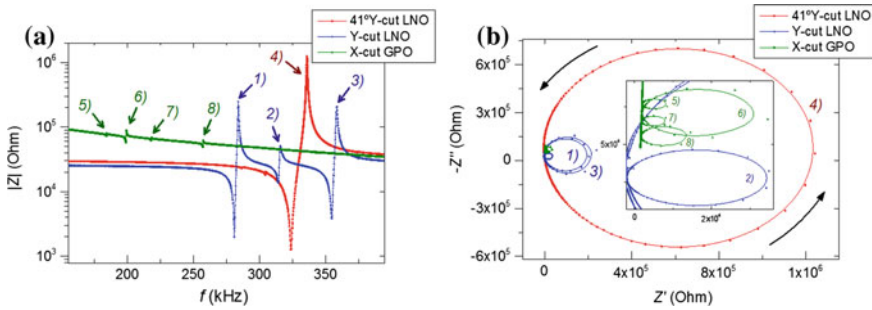


Fig. 7.12 Impedance spectra of the 41°Y-cut LNO, Y-cut LNO and X-cut GPO single-crystals showing its characteristic EM resonance ($|Z| \rightarrow 0$) and anti-resonance ($|Z| \rightarrow \infty$) modes labeled as (1)–(8) and depicted as: **a** the absolute value of the impedance $|Z|$ versus f and; **b** Nyquist plots of the impedance ($-Z''$ vs. Z'). In the last case, the *arrows* indicate the direction of the increasing frequency and the *inset* shows in detail the small loops associated with the weak resonance modes of the Y-cut LNO and X-cut GPO crystals

Another important observation is that the difference between the anti-resonant and resonant frequencies of the 41°Y-cut LNO is much larger than in the other crystals which indicate an enhanced effective EM coupling factor (k_{eff}) and consequently a more efficient conversion of energy [85]. The Nyquist plots show us how the real and imaginary parts of the impedance of the PEs change with the frequency close to a certain resonance mode. Thus we see that, as the frequency increases, the imaginary part of Z starts to increase up to a maximum value where the resonance frequency is ca. attained. After this, the imaginary part starts to drop to zero while the real part of Z starts to increase from a very low positive value up to a maximum close to the anti-resonance frequency. After this frequency, the real part returns to its initial positive value while the imaginary part decreases down to a negative minimum and subsequently returns to its initial value. Each of these resonance modes therefore form a closed loop in the Nyquist plot. More intense resonances in general thus give rise to wider loops and larger resonance peaks. To identify each acoustic resonant mode we again implemented in Matlab® a two-dimensional finite element-method in order to simulate the results [65, 66]. These calculations clearly proved that the resonant peaks observed correspond to different types of in-plane contour resonance modes. The obtained modes are thus labeled in Fig. 7.12 as (1)–(8) and depicted in Fig. 7.13c. To summarize this part, the frequency and $|Z|$ amplitude associated with each anti-resonant mode is listed next: (1) $f = 284.0$ kHz; $|Z| = 246$ kOhm; (2) $f = 315.8$ kHz; $|Z| = 51$ kOhm; (3) $f = 358.6$ kHz; $|Z| = 205$ kOhm; (4) $f = 336.1$ kHz; $|Z| = 1.25$ MOhm; (5) $f = 184.8$ kHz; $|Z| = 80$ kOhm; (6) $f = 199.3$ kHz; $|Z| = 90$ kOhm; (7) $f = 218.4$ kHz; $|Z| = 69$ kOhm; (8) $f = 257.5$ kHz; $|Z| = 63$ kOhm.

The dynamic ME effects (α_{E31} and α_{E32} components) were subsequently measured for the three composites as a function of the frequency of the AC magnetic field. The measurements were performed in the range from 20 Hz–600 kHz, with a fixed bias field of $H = 25$ Oe and a modulation field amplitude of $\delta H = 0.1$ Oe. The

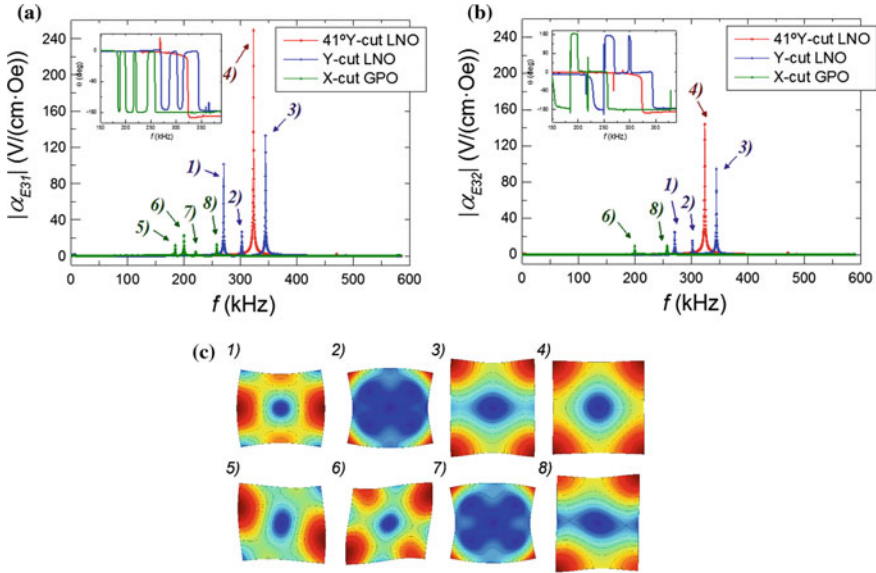


Fig. 7.13 **a** α_{E31} and **b** α_{E32} direct dynamic ME effect measured in tri-layered composites consisting of Metglas and LNO and GPO as a function of the modulation frequency with $H = 25$ Oe and $\delta H = 0.1$ Oe [76]. The various resonant peaks seen here are labeled (1)–(8). The insets in each graph shows the variation of the phase of the ME voltage coefficients (in degrees) as a function of the frequency. **c** Spatial distribution of the in-plane relative displacement field and deformation associated with each type of contour EM resonance mode. Here, redder regions correspond to larger relative displacement amplitudes. The deformation of the crystals are largely exaggerated for the sake of clarity

obtained results are depicted in Fig. 7.13a, b. Here, we can again identify the existence of multiple high-amplitude peaks in the ME response of the samples. By taking into account the sound velocity for the propagation of longitudinal waves in these crystals, of the order of 6.5×10^5 cm/s [61], and their dimensions we conclude that the observed peaks in the kHz range can be attributed to different types of in-plane contour acoustic modes.

With a bias field applied in the X direction (α_{E31} mode), for the case of the composite with the 41° Y-cut LNO crystal a single and very intense ME peak of up to 249.0 V/(cm·Oe) was observed at a frequency of 323.1 kHz. For the sample with the Y-cut LNO crystal, on the other hand, three different smaller peaks were observed in this range. This clearly illustrates how the anisotropic nature of the material constants takes an important part in the determination of which kinds of EM modes may or may not be excited under certain conditions. Consequently we conclude that the anisotropic nature of the PE crystals is even more noticeable in the resonant regime in relation to the quasi-static. In the structure with the Y-cut LNO crystal, the largest peak occurs at approximately 344.3 kHz and takes the value of 132.9 V/(cm·Oe). The other two peaks appear at 270.1 and 302.3 kHz and reach heights of 101.1 and 26.8 V/(cm·Oe), respectively. In the GPO sample we

observed four different resonance modes associated with comparatively smaller ME coefficients. The largest resonant effect here is of 23.2 V/(cm·Oe), occurring at 199.7 kHz. The other three peaks take values of 12.0, 5.0 and 13.0 V/(cm·Oe) and are excited at frequencies of 184.3, 220.5 and 257.9 kHz, respectively. Furthermore we note that all of the aforementioned peaks are associated with a characteristic sudden decrease in phase by ca. 180° as it can be seen in the inset of Fig. 7.13a. In this case the ME resonance peaks are all followed by a change of phase from 0° down to -180° and therefore the imaginary part of the ME coefficients have peaks with negative values in resonance. A comparison with the impedance of the crystals in Fig. 7.12 demonstrates that the same number of resonant modes can be identified in both experiments and that the frequencies and amplitudes of the resonant ME effects in the composites are closely related to the frequencies and amplitudes of the anti-resonant EM modes in the PEs. Thus we conclude that they must correspond to the same type of resonance patterns. This is the case because, as the impedance of the PE crystals is maximized in the anti-resonant mode, its capacitance and longitudinal effective dielectric constant (ϵ) is consequently minimized which results in a large enhancement of the direct voltage ME effect (increase in the d/ϵ ratio) [86].

Having obtained a good agreement between the simulated and experimental values of the anti-resonance frequencies, with relative errors inferior to 4 %, the spatial distribution of the relative displacement fields for each mode can then be plotted as shown in Fig. 7.13c. Thus, we see that the three resonance modes observed in the Y-cut LNO crystal correspond to the three contour acoustic modes (where the in-plane components of the displacement fields do not change significantly in the Z direction and the out-of-plane displacement u_3 is null) dubbed as (1), (2) and (3). We can identify mode (1) as an extensional mode closely related to type I, as labeled by the IRE standard [67], and mode (3) as an extensional mode of type I. In the 41°Y-cut LNO crystal, the observed single resonance (4) corresponds to an extensional mode of type III which is a very symmetric almost isotropic mode. This seems to suggest that remarkably strong resonance modes can be excited in PE crystals, whose geometric symmetry coincides in some way with the symmetry of its anisotropic material constants. This is the case for the 41°Y-cut square-shaped crystal, which is associated with almost equal in-plane d_{31} and d_{32} PE coefficients as well as c_{11}^E and c_{22}^E elastic stiffness constants. By comparison with the properties of some bulk tri-layered composites found in the literature with equivalent structures but employing different compounds, we conclude that the 249 V/(cm·Oe) coefficient observed in the 41°Y-cut LNO sample is one of the largest ever found in ME 2-2 bulk tri-layered structures, being even larger than the 175 V/(cm·Oe) value measured in a Permendur/Quartz/Permendur system [18]. It is also remarkably larger than those found in lead-based PMN-PT (70 V/(cm·Oe)) and PZT (110 V/(cm·Oe)) composites with Permendur [22]. In the X-cut GPO piezocrystal, the first two modes at 184.3 and 199.7 kHz and the fourth one at 257.9 kHz were identified as different kinds of contour shear modes. The first two modes, (5) and (6), and the (8) respectively resemble variations of the modes (1) and (3) in the Y-cut crystal with the addition of an in-plane shear component. The third smallest mode at

220.5 kHz, labeled (7), is characterized by an oscillatory displacement of the vertexes of the crystal in a way similar to mode (2) in the Y-cut LNO piezocrystal.

When a bias field of $H = 25$ Oe was applied in the Y direction instead of X (α_{E32} mode) we obtained the results indicated in Fig. 7.13b. The observed peaks are in general associated with a drop in amplitude in relation to α_{E31} which proves that the ME effects under resonance conditions are also strongly affected by the direction of the applied bias field. The most noticeable change here is the large decrease in amplitude or even disappearance of some of the resonant modes observed in the previous measurement. This is the case of the modes labelled as (5), (7) and (1). In order to explain this we note that these modes are mainly characterized by large elastic displacements in the X direction of the crystals as shown in Fig. 7.13c. Since the Metglas layer tends to expand mainly in the direction of the applied bias field we thus conclude that a magnetic field applied in the Y direction will induce only a small straining of this layer in the X direction. This will thus constrain the capacity of the thin Metglas foil to excite the corresponding EM modes of the PE phases. Additionally we note that the modes labelled as (3), (6) and (8), which are characterized by large displacements in the Y direction tend to be less affected by the change in the direction of the applied bias. Nevertheless the reason for the decrease observed in the amplitude of the mode (4) is not very clear. Furthermore we see that the phase of all of the ME signals still drops by ca. 180° during resonance but now we notice that outside of resonance conditions the phase of the ME effects for the GPO and Y-cut LNO samples is reversed just like in the quasi-static case. Therefore the imaginary part of the ME coefficients will have peaks with positive values in resonance. This kind of behavior has also been observed e.g. in [87].

From a theoretical point of view, considering only the linear elastic properties of the PE crystals and solving their eigenvalue equations of motion under traction-free boundary conditions, several resonance modes in addition to the ones observed in the measurements can be predicted. We therefore conclude that the pattern and natural frequency of these normal modes are mainly determined by the elastic coefficients of the crystals as well as their mass density and geometry. The excitation or not of some of these modes in the ME measurements, under specific mechanical and electrical boundary conditions, is then driven by the PE effect and thus depends on its anisotropic coefficients. While strong ME effects were observed for the extensional EM resonance modes in the samples with LNO, much weaker effects were seen for the asymmetrical shear modes in the one with GPO. These shear modes arise primarily because of non-null stiffness coefficients c_{16}^E in the X-cut crystal which couple in-plane normal and shear type stresses and strains. Having seen this, we note that extensional normal modes, similar to the ones identified in the LNO crystals, as well as more symmetrical shear modes can also be solutions of the equations of motion in crystals of GPO e.g. with a Z- or Y-cut, since here we have $c_{16}^E = c_{26}^E = 0$. Nevertheless, the form of its corresponding PE tensors in principle doesn't permit the ME excitation of the extensional modes in L-T tri-layered composites, since in these cases we have both null d_{31} and d_{32} components. In conclusion, we see that even though a large ME effect may be predicted for a given

anisotropic composite under quasi-static conditions, under resonant conditions the picture changes radically. Thus, in this case, a more sophisticated investigation must be carried out taking into account further parameters such as the relation between the crystal orientation and the geometry of the composite.

In summary, in this experimental part we investigated the relation between the cut orientation of the piezocrystals and respective in-plane anisotropic ME response of the corresponding tri-layered composites. By precisely selecting this cut direction, systems with different relations between perpendicular α_{E31} and α_{E32} ME coefficients could be designed, thus finding applications in specific orientation-sensitive devices. A composite with a Y-cut LNO crystal, for example, was shown to operate closely to the anisotropic unipolar regime ($\alpha_{E31} > 0$ and $\alpha_{E32} = 0$), and one with a 41° -Y-cut LNO crystal closely to the in-plane isotropic regime ($\alpha_{E31} = \alpha_{E32}$). Figure 7.14a further illustrates the results of calculated quasi-static α_{E31} and α_{E32} coefficients as a function of the LNO crystal cut angle in the YZ plane in relation to the Y axis, i.e. the θ angle in the standard notation (YXl) θ or $\theta = 90^\circ + \beta$ in the Euler angles scheme. According to the calculations, the anisotropic unipolar regime and the in-plane isotropic regime should be observed for LNO crystals with cut angles of 2° -Y and 45° -Y, respectively. From this point of view, other cuts could also be interesting, such as the 162.1° -Y-cut LNO, corresponding to an anisotropic bipolar regime ($\alpha_{E31} = -\alpha_{E32}$), and the 129° -Y-cut LNO, corresponding to the maximum expected ME voltage coefficient as seen in Fig. 7.10a. Also, Fig. 7.14b depicts the calculated ME voltage coefficients as a function of the relative thickness ratio between the PE and MS phases using the same formalism. This calculation was made for some of the most interesting LNO crystal cuts. From this we see that a decrease in the thickness of the PE layer results in more stress being transferred to it from the MS and, consequently, in an increase of the ME effect. However, since the detected voltage is proportional to the PE layer thickness, the thinner the layer is, the lower the output signal will be. Therefore, taking into account that any measuring circuit has its own input noise, the maximal signal-to-noise ratio should be observed for a finite ferroelectric film thickness.

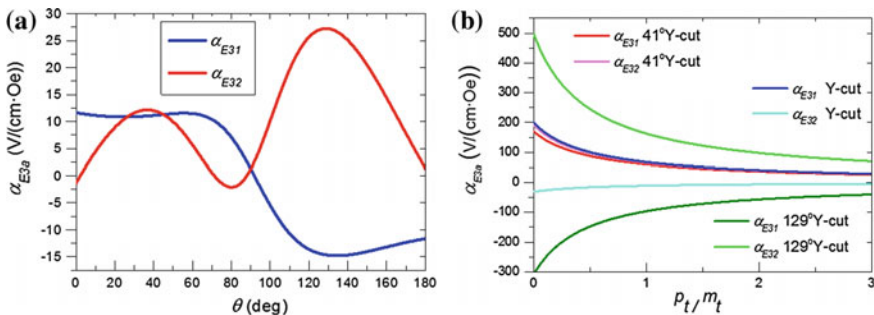


Fig. 7.14 **a** Calculated in-plane quasi-static ME voltage coefficients as a function of the θ piezocrystal cut angle (measured from the Y axis). **b** ME coefficients for different crystal cuts as a function of the PE/MS relative thickness ratio (ρ_t/m_t) [30]

7.4 Conclusions

In this chapter we have presented an experimental study of the direct and converse magnetoelectric (ME) effects in tri-layered composites based on Metglas and piezoelectric (PE) single-crystals of lithium niobate and gallium phosphate in comparison with laminates based on the popular piezoelectric PMN-PT. In the first part, various techniques used in the measurement of the ME effect were explored, with special emphasis on the dynamic lock-in technique employed in our experiments. In this technique the sample is subjected to two magnetic fields, a DC bias and an AC modulation field. The AC voltage generated across the sample is subsequently measured in a lock-in amplifier. These measurements can then be performed as a function of the magnetic bias field or the frequency of the modulation field. The formalism describing this technique was presented, and we showed how the different order ME coefficients can be extracted from the measurements of the voltages synchronized with the fundamental and harmonic frequencies of the exciting signal. Subsequently we presented a custom-made setup used by us to measure the dynamic ME effect. Its scheme and characteristics as well as ways to reduce the noise and the parasitic induction voltage were explored.

In the second part we introduced a comparative study between the direct and converse ME effects in tri-layered composites of the type Metglas/PE/Metglas based on single crystals of LiNbO_3 (LNO) and [011]-poled PMN-PT bonded with a cyanoacrylate glue. In the quasi-static regime we showed that the transversal direct ME effects had comparable magnitudes in both LNO and PMN-PT samples, which was due to comparable ratios between piezoelectric and dielectric coefficients of both crystals. The converse ME effects, on the other hand, were shown to be much stronger in the sample with the PMN-PT crystal since, according to the theory, this effect depends only on the piezoelectric constants which are much larger in this case. We also presented the results of the direct ME measurements in the resonant regime. Here we found an even larger ME effect peak in the composite with the 41° Y-cut LNO than in the one with PMN-PT. We therefore conclude that lead-free single-crystals like LNO might constitute a good alternative to PMN-PT in terms of practical ME applications.

Subsequently we describe a study of the anisotropic direct ME and electromechanical (EM) properties in tri-layered composites featuring Metglas and differently cut PE single crystals of LNO and GaPO_4 (GPO) bonded with epoxy. Results of the quasi-static measurements were shown to vary strongly with the direction of the applied transverse magnetic fields and the crystallographic orientation of the PE. In greater detail, the 41° Y-cut LNO crystal was shown to produce an in-plane isotropic ME response while the Y-cut LNO and X-cut GPO generated an in-plane unipolar effect.

In the resonant regime, several in-plane contour EM resonant peaks were observed in the ME spectrum. Here we saw how strongly the anisotropic nature of the PE crystals influences the excitation of certain contour acoustic resonance modes. So, e.g., three distinct resonance modes were observed in the system

featuring the Y-cut LNO crystal, whereas a single one was observed in the composite with the 41°Y-cut LNO one. A very intense single peak exhibiting a ME coefficient of up to 249 V/(cm·Oe) was detected in the sample with the 41°Y-cut LNO crystal. In order to predict, which kinds of modes could be excited under given conditions and to identify such modes by comparison with simulated results, we employed impedance measurements, thus clarifying the relation between the anisotropic constants and the excitation of such peaks. The aforementioned large symmetric peak was therefore shown to be related to the in-plane isotropic properties of the crystal, so that a very symmetric and high-amplitude resonance mode was generated. In the GPO sample, four weak contour asymmetrical shear modes of resonance were identified, with the largest having a response of up to 23.2 V/(cm·Oe) and appearing at a frequency of 199.7 kHz.

In conclusion, we were able to identify relatively large anisotropic ME effects in composites based on PE single-crystals which were in good agreement with the theory. In principle, such ME responses can be further enhanced through the optimization of the volume ratio and the coupling between layers. Finally we showed how the control of the crystal orientation can be used to greatly enhance the anisotropic ME effects in composites. The selection of the crystal orientation should therefore allow one to engineer almost any desired anisotropic properties for some given application.

Acknowledgments This work was developed in the scope of the projects I3N/FSCOSD (Ref. FCT UID/CTM/50025/2013), CICECO—Aveiro Institute of Materials—POCI-01-0145-FEDER-007679 (FCT Ref. UID /CTM /50011/2013), and RECI/FIS-NAN/0183/2012 (FCOMP-01-0124-FEDER-027494), financed by national funds through the FCT/MEC and when applicable cofinanced by FEDER under the PT2020 Partnership Agreement. J.V.V. and A.A.T. thank for the FCT grants SFRH/BD/89097/2012 and SFRH/BPD/74086/2010, respectively. N.A.S. acknowledges support by NUST “MISiS” through grant no. K3-2015-003.

References

1. C.-W. Nan, M.I. Bichurin, S. Dong, D. Viehland, G. Srinivasan, Multiferroic magnetolectric composites: historical perspective, status, and future directions. *J. Appl. Phys.* **103**(3), 031101–031135 (2008)
2. M. Fiebig, Revival of the magnetolectric effect. *J. Phys. D Appl. Phys.* **38**(8), R123–R152 (2005)
3. J. Ma, J. Hu, Z. Li, C.-W. Nan, Recent progress in multiferroic magnetolectric composites: from bulk to thin films. *Adv. Mater.* **23**(9), 1062–1087 (2011)
4. J. Ryu, S. Priya, K. Uchino, H.-E. Kim, Magnetolectric effect in composites of magnetostrictive and piezoelectric materials. *J. Electroceram.* **8**(2), 107–119 (2002)
5. M. Bichurin, D. Viehland, G. Srinivasan, Magnetolectric interactions in ferromagnetic-piezoelectric layered structures: phenomena and devices. *J. Electroceram.* **19**(4), 243–250 (2007)
6. Y. Wang, J. Hu, Y. Lin, C.-W. Nan, Multiferroic magnetolectric composite nanostructures. *NPG Asia Mater.* **2**(2), 61–68 (2010)
7. J. Zhai, Z. Xing, S. Dong, J. Li, D. Viehland, Magnetolectric laminate composites: an overview. *J. Am. Ceram. Soc.* **91**(2), 351–358 (2008)

8. W. Eerenstein, N.D. Mathur, J.F. Scott, Multiferroic and magnetoelectric materials. *Nature* **442**(7104), 759–765 (2006)
9. D.R. Tilley, J.F. Scott, Frequency dependence of magnetoelectric phenomena in BaMnF₄. *Phys. Rev. B* **25**(5), 3251–3260 (1982)
10. M.I. Bichurin, V.M. Petrov, O.V. Ryabkov, S.V. Averkin, G. Srinivasan, Theory of magnetoelectric effects at magnetoacoustic resonance in single-crystal ferromagnetic-ferroelectric heterostructures. *Phys. Rev. B* **72**(6), 060408–060411 (2005)
11. M.I. Bichurin, V.M. Petrov, Y.V. Kiliba, G. Srinivasan, Magnetic and magnetoelectric susceptibilities of a ferroelectric/ferromagnetic composite at microwave frequencies. *Phys. Rev. B* **66**(13), 134404–134413 (2002)
12. G. Srinivasan, Magnetoelectric composites. *Annu. Rev. Mater. Res.* **40**, 153–178 (2010)
13. G. Sreenivasulu, S.K. Mandal, S. Bandekar, V.M. Petrov, G. Srinivasan, Low-frequency and resonance magnetoelectric effects in piezoelectric and functionally stepped ferromagnetic layered composites. *Phys. Rev. B* **84**(14), 144426–144431 (2011)
14. S.N. Babu, T. Bhimasankaram, S.V. Suryanarayana, Magnetoelectric effect in metal-PZT laminates. *Bull. Mater. Sci.* **28**(5), 419–422 (2004)
15. C.P. Zhao, F. Fang, W. Yang, A dual-peak phenomenon of magnetoelectric coupling in laminated Terfenol-D/PZT/Terfenol-D composites. *Smart Mater. Struct.* **19**(12), 125004–125010 (2010)
16. J. Ryu, A.V. Carazo, K. Uchino, H.-E. Kim, Magnetoelectric properties in piezoelectric and magnetostrictive laminate composites. *Jpn. J. Appl. Phys.* **40**(8), 4948–4951 (2001)
17. H. Greve, E. Woltermann, H.-J. Quenzer, B. Wagner, E. Quandt, Giant magnetoelectric coefficients in (Fe₉₀Co₁₀)₇₈Si₁₂B₁₀-AlN thin film composites. *Appl. Phys. Lett.* **96**(18), 182501–182503 (2010)
18. G. Sreenivasulu, V.M. Petrov, L.Y. Fetisov, Y.K. Fetisov, G. Srinivasan, Magnetoelectric interactions in layered composites of piezoelectric quartz and magnetostrictive alloys. *Phys. Rev. B* **86**(21), 214405–214411 (2012)
19. Y. Shen, K.L. McLaughlin, J. Gao, M. Li, J. Li, D. Viehland, Effective optimization of magnetic noise for a Metglas/Pb(Zr, Ti)O₃ magnetoelectric sensor array in an open environment. *Mater. Lett.* **91**, 307–310 (2013)
20. Y. Wang, D. Gray, J. Gao, D. Berry, M. Li, J. Li, D. Viehland, H. Luo, Improvement of magnetoelectric properties in Metglas/Pb(Mg_{1/3}Nb_{2/3})O₃-PbTiO₃ laminates by poling optimization. *J. Alloys Compd.* **519**, 1–3 (2012)
21. R. Viswan, D. Gray, Y. Wang, Y. Li, D. Berry, J. Li, D. Viehland, Strong magnetoelectric coupling in highly oriented ZnO films deposited on Metglas substrates. *Phys. Status Solidi-R* **5**(10–11), 391–393 (2011)
22. G. Sreenivasulu, L.Y. Fetisov, Y.K. Fetisov, G. Srinivasan, Piezoelectric single crystal langatate and ferromagnetic composites: Studies on low-frequency and resonance magnetoelectric effects. *Appl. Phys. Lett.* **100**(5), 052901–052904 (2012)
23. G. Sreenivasulu, P. Qu, E. Piskulich, V.M. Petrov, Y.K. Fetisov, A.P. Nosov, H. Qu, G. Srinivasan, Shear strain mediated magneto-electric effects in composites of piezoelectric lanthanum gallium silicate or tantalate and ferromagnetic alloys. *Appl. Phys. Lett.* **105**(3), 032409–032412 (2014)
24. J.-P. Rivera, A short review of the magnetoelectric effect and related experimental techniques on single phase (multi-) ferroics. *Eur. Phys. J. B* **71**(3), 299–313 (2009)
25. D.C. Lupascu, H. Wende, M. Etier, A. Nazrabi, I. Anusca, H. Trivedi, V.V. Shvartsman, J. Landers, S. Salamon, C. Schmitz-Antoniak, Measuring the magnetoelectric effect across scales. *GAMM-Mitteilungen* **38**(1), 25–74 (2015)
26. G.V. Duong, R. Groessinger, M. Schoenhardt, D. Bueno-Basques, The lock-in technique for studying magnetoelectric effect. *J. Mag. Mag. Mat.* **316**(2), 390–393 (2007)
27. M.M. Kumar, A. Srinivas, S.V. Suryanarayana, G.S. Kumar, T. Bhimasankaram, An experimental setup for dynamic measurement of magnetoelectric effect. *Bull. Mater. Sci.* **21**(3), 251–255 (1998)

28. Y.J. Wang, J.Q. Gao, M.H. Li, Y. Shen, D. Hasanyan, J.F. Li, D. Viehland, A review on equivalent magnetic noise of magnetolectric laminate sensors. *Phil. Trans. R. Soc. A* **372** (2009), 20120455 (2014)
29. Y.K. Fetisov, K.E. Kamentsev, A.Y. Ostashchenko, G. Srinivasan, Wide-band magnetolectric characterization of a ferrite-piezoelectric multilayer using a pulsed magnetic field. *Solid State Commun.* **132**(1), 13–17 (2004)
30. A.A. Timopheev, J.V. Vidal, A.L. Kholkin, N.A. Sobolev, Direct and converse magnetolectric effects in Metglas/LiNbO₃/Metglas trilayers. *J. Appl. Phys.* **114**(4), 044102–044108 (2013)
31. S. Priya, R. Islam, S. Dong, D. Viehland, Recent advancements in magnetolectric particulate and laminate composites. *J. Electroceram.* **19**(1), 149–166 (2007)
32. M. Vopsarou, J. Blackburn, M.G. Cain, Emerging technologies and opportunities based on the magneto-electric effect in multiferroic composites. *MRS Proc.* **1161**, 1161-I05-04 (2009)
33. R.C. Kambale, D.-Y. Jeong, J. Ryu, Current status of magnetolectric composite thin/thick films. *Adv. Cond. Matter Phys.* **2012**, 824643 (2012)
34. J. More-Chevalier, C. Cibert, R. Bouregba, G. Poullain, Eddy currents: a misleading contribution when measuring magnetolectric voltage coefficients of thin film devices. *J. Appl. Phys.* **117**(15), 154104–154110 (2015)
35. D.A. Burdin, D.V. Chashin, N.A. Ekonomov, L.Y. Fetisov, Y.K. Fetisov, G. Sreenivasulu, G. Srinivasan, Nonlinear magneto-electric effects in ferromagnetic-piezoelectric composites. *J. Mag. Mat.* **358–359**, 98–104 (2014)
36. Y.K. Fetisov, D.A. Burdin, D.V. Chashin, N.A. Ekonomov, High-Sensitivity Wideband Magnetic Field Sensor Using Nonlinear Resonance Magnetolectric Effect. *Sens. J. IEEE*, **14** (7), 2252–2256 (2014)
37. Y. Chen, S.M. Gillette, T. Fitchorov, L. Jiang, H. Hao, J. Li, X. Gao, A. Geiler, C. Vittoria, V. G. Harris, Quasi-one-dimensional miniature multiferroic magnetic field sensor with high sensitivity at zero bias field. *Appl. Phys. Lett.* **99**(4), 042505 (2011)
38. J. Gao, Z. Wang, Y. Shen, M. Li, Y. Wang, P. Finkel, J. Li, D. Viehland, Self-powered low noise magnetic sensor. *Mater. Lett.* **82**, 178–180 (2012)
39. J. Gao, Y. Shen, P. Finkel, J. Blottman, J. Li, D. Viehland, Geomagnetic field tuned frequency multiplication in Metglas/Pb(Zr, Ti)O₃ heterostructure. *Mater. Lett.* **88**, 47–50 (2012)
40. N.X. Sun, G. Srinivasan, Voltage control of magnetism in multiferroic heterostructures and devices. *Spin* **02**(03), 12240004 (2012)
41. C.A. Vaz, Electric field control of magnetism in multiferroic heterostructures. *J. Phys.: Cond. Mat.* **24**(33), 333201 (2012)
42. M. Li, Y. Wang, D. Hasanyan, J. Li, D. Viehland, Giant converse magnetolectric effect in multi-push-pull mode Metglas/Pb(Zr, Ti)O₃/Metglas laminates. *Appl. Phys. Lett.* **100**(13), 132904–132906 (2012)
43. S. Dong, J. Zhai, F. Bai, J.-F. Li, D. Viehland, Push-pull mode magnetostrictive/piezoelectric laminate composite with an enhanced magnetolectric voltage coefficient. *Appl. Phys. Lett.* **87** (6), 062502–062504 (2005)
44. S.-E. Park, T.R. Shrout, Ultrahigh strain and piezoelectric behavior in relaxor based ferroelectric single crystals. *J. Appl. Phys.* **82**(4), 1804 (1997)
45. C.-S. Park, K.-H. Cho, M.A. Arat, J. Evey, S. Priya, High magnetic field sensitivity in Pb(Zr, Ti)O₃-Pb(Mg_{1/3}Nb_{2/3})O₃ single crystal/Terfenol-D/Metglas magnetolectric laminate composites. *J. Appl. Phys.* **107**(9), 094109 (2010)
46. S. Dong, J. Cheng, J.F. Li, D. Viehland, Enhanced magnetolectric effects in laminate composites of Terfenol-D/Pb(Zr, Ti)O₃ under resonant drive. *Appl. Phys. Lett.* **83**(23), 4812–4814 (2003)
47. S. Dong, J.-F. Li, D. Viehland, Ultrahigh magnetic field sensitivity in laminates of TERFENOL-D and Pb(Mg_{1/3}Nb_{2/3})O₃-PbTiO₃ crystals. *Appl. Phys. Lett.* **83**(11), 2265–2267 (2003)

48. M. Bichurin, V. Petrov, A. Zakharov, D. Kovalenko, S.C. Yang, D. Maurya, V. Bedekar, S. Priya, Magnetolectric interactions in lead-based and lead-free composites. *Materials* **4**(4), 651–702 (2011)
49. H.F. Tian, T.L. Qu, L.B. Luo, J.J. Yang, S.M. Guo, H.Y. Zhang, Y.G. Zhao, J.Q. Li, Strain induced magnetolectric coupling between magnetite and BaTiO₃. *Appl. Phys. Lett.* **92**(6), 063507–063509 (2008)
50. P. Yang, K. Zhao, Y. Yin, J.G. Wan, J.S. Zhu, Magnetolectric effect in magnetostrictive/piezoelectric laminate composite Terfenol-D/LiNbO₃ [(zxtw) – 129°/30°]. *Appl. Phys. Lett.* **88** (17), 172903–172905 (2006)
51. J.V. Vidal, A.A. Timopheev, A.L. Kholkin, N.A. Sobolev, Anisotropy of the magnetolectric effect in tri-layered composites based on single-crystalline piezoelectrics. *Vacuum* 1–7
52. M. Yachi, M. Ono, The third overtone resonator using 36° rotated Y cut LiNbO₃ crystal, in *Ultrasonics Symposium, 1995. Proceedings. 1995 IEEE*, vol 2, p. 1003 (1995)
53. L.E. Myers, R.C. Eckardt, M.M. Fejer, R.L. Byer, W.R. Bosenberg, J.W. Pierce, Quasi-phase-matched optical parametric oscillators in bulk periodically poled LiNbO₃. *J. Opt. Soc. Am. B* **12**(11), 2102–2116 (1995)
54. A. Heinrich, A.L. Hörner, A. Wixforth, B. Stritzker, Pulsed laser deposition of La_{0.67}Ca_{0.33}MnO₃ thin films on LiNbO₃ and surface acoustic wave studies. *Thin Solid Films* **510**(1–2), 77–81 (2006)
55. A. Kawamata, H. Hosaka, T. Morita, Non-hysteresis and perfect linear piezoelectric performance of a multilayered lithium niobate actuator. *Sens. Actuators A Phys.* **135**(2), 782–786 (2007)
56. G. Matsunami, A. Kawamata, H. Hosaka, T. Morita, Multilayered LiNbO₃ actuator for XY-stage using a shear piezoelectric effect. *Sens. Actuators A Phys.* **144**(2), 337–340 (2008)
57. L. Dreher, M. Weiler, M. Pernpeintner, H. Huebl, R. Gross, M.S. Brandt, S.T.B. Goennenwein, Surface acoustic wave driven ferromagnetic resonance in nickel thin films: theory and experiment. *Phys. Rev. B* **86**(13), 134415 (2012)
58. N. Obata, T. Kawahata, R. Suzuki, K. Nishimura, H. Uchida, M. Inoue, Fabrication and properties of InSb films with ion-beam sputtering for use in the amplification of magneto-surface-acoustic waves. *Phys. Stat. Sol. (a)* **201**(8), 1973–1975 (2004)
59. H.-Y. Kuo, A. Slinger, K. Bhattacharya, Optimization of magnetolectricity in piezoelectric-magnetostrictive bilayers. *Smart Mater. Struct.* **19**(12), 125010–125022 (2010)
60. T. Wu, A. Bur, J.L. Hockel, K. Wong, T.-K. Chung, G.P. Carman, Electrical and mechanical manipulation of ferromagnetic properties in polycrystalline nickel thin film. *IEEE Magn. Lett.* **2**, 6000104–6000104 (2011)
61. R.S. Weis, T.K. Gaylord, Lithium niobate: Summary of physical properties and crystal structure. *Appl. Phys. A Mater. Sci. Process.* **37**(4), 191–203 (1985)
62. P. Han, W. Yan, J. Tian, X. Huang, H. Pan, Cut directions for the optimization of piezoelectric coefficients of lead magnesium niobate–lead titanate ferroelectric crystals. *Appl. Phys. Lett.* **86** (5), 052902–052904 (2005)
63. A.W. Warner, M. Onoe, G.A. Coquin, Determination of elastic and piezoelectric constants for crystals in class (3 m). *J. Acoust. Soc. Am.* **42**(6), 1223–1231 (1967)
64. W. Yue, J. Yi-jian, Crystal orientation dependence of piezoelectric properties in LiNbO₃ and LiTaO₃. *Opt. Mater.* **23**(1–2), 403–408 (2003)
65. C. Zhang, W. Chen, J. Li, J. Yang, Two-dimensional analysis of magnetolectric effects in multiferroic laminated plates. *IEEE Trans. Ultrason. Ferroelectr. Freq. Control* **56**(5), 1046–1053 (2009)
66. C. Zhang, W. Chen, C. Zhang, Two-dimensional theory of piezoelectric plates considering surface effect. *Eur. J. Mech.—A/Solid.* **41**, 50–57 (2013)
67. IRE Standards on Piezoelectric Crystals: Determination of the Elastic, Piezoelectric, and Dielectric Constants-The Electromechanical Coupling Factor, 1958. *Proc. IRE* **46**(4), 764–778 (1958)
68. R. Zhang, B. Jiang, W. Cao, Elastic, piezoelectric, and dielectric properties of multidomain 0.67Pb(Mg_{1/3}Nb_{2/3})O₃-0.33PbTiO₃ single crystals. *J. Appl. Phys.* **90** (7), 3471–3475 (2001)

69. M.I. Bichurin, V.M. Petrov, G. Srinivasan, Theory of low-frequency magnetolectric coupling in magnetostrictive-piezoelectric bilayers. *Phys. Rev. B* **68**(5), 054402–054414 (2003)
70. Z. Huang, Theoretical modeling on the magnetization by electric field through product property. *J. Appl. Phys.* **100**(11), 114104–114108 (2006)
71. M. Bichurin, V. Petrov, *Modeling of Magnetolectric Effects in Composites*, Springer (2014), 9401791562, 9789401791564
72. G. Wu, T. Nan, R. Zhang, N. Zhang, S. Li, N.X. Sun, Inequivalence of direct and converse magnetolectric coupling at electromechanical resonance. *Appl. Phys. Lett.* **103**(18), 182905–182909 (2013)
73. J.-P. Zhou, Y.-J. Ma, G.-B. Zhang, X.-M. Chen, A uniform model for direct and converse magnetolectric effect in laminated composite. *Appl. Phys. Lett.* **104**(20), 202904–202908 (2014)
74. P. Davulis, J.A. Kosinski, M.P. da Cunha, GaPO₄ Stiffness and Piezoelectric Constants Measurements using the Combined Thickness Excitation and Lateral Field Technique, in *International Frequency Control Symposium and Exposition*, pp. 664–669 (2006)
75. W. Wallnöfer, P.W. Krempf, A. Asenbaum, Determination of the elastic and photoelastic constants of quartz-type GaPO₄ by Brillouin scattering. *Phys. Rev. B* **49**(15), 10075–10080 (1994)
76. J.V. Vidal, A.A. Timopheev, A.L. Kholkin, N.A. Sobolev, Anisotropy of the magnetolectric effect in tri-layered composites based on single-crystalline piezoelectrics. *Vacuum* **122**, Part B, 286–292 (2015)
77. F. Fang, C. Zhao, W. Yang, Thickness effects on magnetolectric coupling for Metglas/PZT/Metglas laminates. *Sci. China Phys. Mech. Astron.* **54**(4), 581–585 (2011)
78. D. Hasanyan, J. Gao, Y. Wang, R. Viswan, Y.S.M. Li, J. Li, D. Viehland, Theoretical and experimental investigation of magnetolectric effect for bending-tension coupled modes in magnetostrictive-piezoelectric layered composites. *J. Appl. Phys.* **112**(1), 013908–013918 (2012)
79. Y. Wang, D. Hasanyan, M. Li, J. Gao, J. Li, D. Viehland, H. Luo, Theoretical model for geometry-dependent magnetolectric effect in magnetostrictive/piezoelectric composites. *J. Appl. Phys.* **111**(12), 124513–124518 (2012)
80. S. Dong, J. Zhai, J. Li, D. Viehland, Near-ideal magnetolectricity in high-permeability magnetostrictive/piezofiber laminates with a (2-1) connectivity. *Appl. Phys. Lett.* **89**(25), 252904–252906 (2006)
81. R. Tinder, *Tensor Properties of Solids* (Morgan & Claypool, 2007), 9781598293494
82. L.W. Martin, R. Ramesh, Multiferroic and magnetolectric heterostructures. *Acta Mater.* **60** (6–7), 2449–2470 (2012)
83. H.-M. Zhou, Y.-H. Zhou, X.-J. Zheng, Q. Ye, J. Wei, A general 3-D nonlinear magnetostrictive constitutive model for soft ferromagnetic materials. *J. Mag. Mag. Mat.* **321** (4), 281–290 (2009)
84. M. Cochez, J.D. Foulon, A. Ibanez, A. Goiffon, E. Philippot, B. Capelle, A. Zarka, J. Schwartzel, J. Detaint, Crystal growth and characterizations of a quartz-like material: GaPO₄. *J. Phys. IV France*, **04**, C2-183–C2-188 (1994)
85. IEEE Standard on Piezoelectricity, *ANSI/IEEE Std 176–1987*, pp. 1–74 (1988)
86. K.-H. Cho, S. Priya, Direct and converse effect in magnetolectric laminate composites. *Appl. Phys. Lett.* **98**(23), 232904 (2011)
87. D. Rajaram Patil, Y. Chai, R.C. Kambale, B.-G. Jeon, K. Yoo, J. Ryu, W.-H. Yoon, D.-S. Park, D.-Y. Jeong, S.-G. Lee, J. Lee, J.-H. Nam, J.-H. Cho, B.-I. Kim, K. Hoon Kim, Enhancement of resonant and non-resonant magnetolectric coupling in multiferroic laminates with anisotropic piezoelectric properties. *Appl. Phys. Lett.* **102**(6), 062909 (2013)